

Effects of black hole environments on extreme mass-ratio hyperbolic encounters

Ya-Ze Cheng^a, Yan Cao^b, and Yong Tang^{a,c,d}

^a*School of Astronomy and Space Sciences, University of Chinese Academy of Sciences (UCAS), Beijing 100049, China*

^b*School of Physics, Nanjing University, Nanjing 210093, China*

^c*School of Fundamental Physics and Mathematical Sciences,
Hangzhou Institute for Advanced Study, UCAS, Hangzhou 310024, China*

^d*International Center for Theoretical Physics Asia-Pacific, Beijing/Hangzhou, China*

(Dated: November 13, 2024)

Extreme mass-ratio hyperbolic encounters (EMRHEs) around the supermassive black holes will be observable at the future gravitational-wave (GW) detectors in space, such as LISA and Taiji. Here we consider such EMRHEs in the presence of surrounding matter distribution including baryonic accretion disk and dark matter (DM) spike, and estimate their effects on the orbital evolution and GW waveforms. We find that large possible impacts come from the gravitational potential of accretion disk, while the influence of DM spike is small. We also illustrate that environments can leave distinctive imprints on the GW waveforms, but resolving such modifications is found to be challenging for LISA-like detectors in the near future.

I. INTRODUCTION

The first detection of gravitational waves has opened a new era of multi-messenger astronomy [1]. Since then, hundreds of GW events has been detected by the LIGO-Virgo-KAGRA collaboration, which are generated during the final stages of stellar-mass compact binary mergers [2–4]. Near future space-based GW interferometers, such as LISA and Taiji, are designed to detect GWs of lower frequencies, thus enabling the exploration of a wider range of GW events, including the inspiral and hyperbolic encounter of extreme mass-ratio binaries [5, 6].

Gravitational bremsstrahlung from the scattering of compact objects (COs) is a potentially important type of GW signals [7, 8]. Different from the gravitational waves radiated by inspiralling binaries, such bremsstrahlung radiation is burst-like, with a relatively short duration and accompanied with linear GW memory, which has been analyzed for binaries in vacuum using the Newtonian approximation [8–13], post-Newtonian or geodesic-based approximation [14–25] and numerical relativity [26]. The detectability and event rate of the GW signals from compact binary hyperbolic encounters have been evaluated in works such as [9, 12, 27, 28]. These signals may already exist in the current observational data of ground-based GW interferometers, although searches so far have not identified them [29, 30]. Furthermore, a large number of unresolved binary encounters can form a specific stochastic gravitational wave background [31–33].

One particularly interesting and realistic type of scattering events is the EMRHE between stellar-mass COs and the supermassive black holes in galaxy centers. The vicinity of a supermassive black hole (SMBH) is likely to host rich and important physical processes that are beyond the reach of direct observations. An indirect messenger is provided by the gravitational waves emitted by small COs orbiting the central BH, whose motion can be affected by the black hole environments gravitationally, thus leaving imprints in their GW waveforms. This possibility has been extensively studied for the inspiraling

extreme or intermediate mass-ratio binaries [6, 34–54]. A similar situation could occur in the case of unbound orbits. But so far only the impact of DM spike has been discussed in the context of intermediate mass-ratio hyperbolic encounters [55].

In this paper, we study the gravitational effects of two types of environments - accretion disk and DM spike - on the orbital evolution and GW waveforms of EMRHEs around SMBHs. EMRHEs are affected by the BH environment mainly through its gravitational potential, whose effect in some cases turn out to be more significant than the relativistic corrections. The influence of DM spike is found to be typically weak, while the presence of accretion disk (in particular the α disk) can have potentially large impacts. We also examine the detectability of gravitational wave signals from EMRHE events in the centers of Milky Way and the nearby galaxy M31, as well as the distinguishability of environmental imprints in the waveforms. We find that events showing distinctive waveform modifications due to the environmental influences are generally beyond the sensitivity range of upcoming LISA-like detectors, while the environmental signatures can be challenging to resolve in the waveforms of more detectable events.

The structure of our paper is as follows. In Sec. II, we present a general framework for the computation of orbital evolution during the hyperbolic encounter. The physical models of DM spike and accretion disk are reviewed in Sec. III, where we also derive the corresponding environmental forces. The orbital evolution in the presence of environments are investigated concretely in Sec. IV and in Sec. V, we calculate and analyze the associated GW waveforms. We give our conclusions in Sec. VI. Throughout this paper, we use the natural units $G = c = \hbar = 1$.

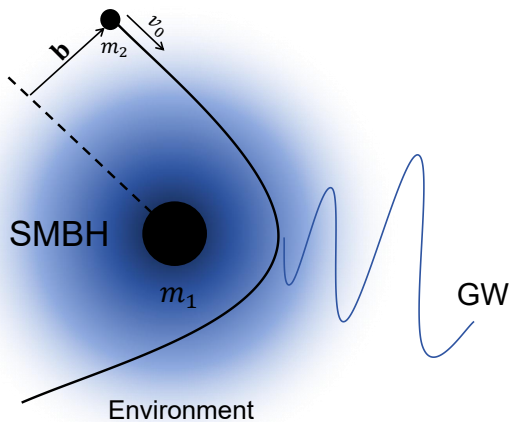


FIG. 1. Sketch of an EMRHE in the presence of BH environment. Burst-like GW is emitted during this process.

II. ORBITAL PARAMETRIZATION AND DYNAMICS

A. Initial condition

We consider a small compact object with mass m_2 scattered by a massive central BH with mass m_1 , as illustrated in Fig. 1. The position vectors of the two bodies are denoted by $\mathbf{r}_{1,2}$ in the center-of-mass (COM) frame, with the relative motion given by $\mathbf{r} = \mathbf{r}_2 - \mathbf{r}_1$ and $\mathbf{v} = \dot{\mathbf{r}}$. In the Newtonian order, this two-body scattering corresponds to a hyperbolic orbit which can be parameterized by six orbital elements $\{a, e, \varphi_0, \phi_0, i, t_0\}$ with respect to a fixed reference plane (see Fig. 2 and also Appendix C), here a is the semi-major axis, e the eccentricity, φ_0 the argument of periastron on the orbital plane, $\phi_0 - \pi/2$ the longitude of the ascending node and i the inclination angle of the orbital plane relative to the reference plane.

Under perturbations, the true orbit will deviate from the Keplerian one¹, but it can always be described with an evolving osculating Keplerian orbit, with the position and velocity matched with the true orbit at any given moment. We shall assume that the initial velocity \mathbf{v}_0 is small enough and the environment only has a finite influence radius, then at sufficiently large distance from the central BH, the motion should be well-approximated by a Keplerian orbit, and the initial state of this scattering

process can be specified by the impact parameter vector $\mathbf{b} = b(\mathbf{e}_r \times \mathbf{e}_z)$ and the relative velocity \mathbf{v}_0 in the asymptotic past, corresponding to an initial osculating orbit with [58]

$$e_0 = e(t=0) = \sqrt{1 + \frac{b^2 v_0^4}{M^2}}, \quad (1)$$

$$a_0 = a(t=0) = \frac{b}{\sqrt{e_0^2 - 1}}, \quad (2)$$

where $M = m_1 + m_2$ is the total mass.

For the numerical computation, it is convenient to use the spherical coordinates (r, θ, ϕ) , in which

$$\mathbf{r} = r \mathbf{e}_r, \quad (3)$$

$$\mathbf{v} = \dot{r} \mathbf{e}_r + r \dot{\theta} \mathbf{e}_\theta + r \sin \theta \dot{\phi} \mathbf{e}_\phi. \quad (4)$$

The Cartesian components of the initial position $\mathbf{r}(t=0)$ and velocity $\mathbf{v}(t=0)$ in the fixed $x'y'z'$ coordinate system (defined in Fig. 2) are fixed by the initial osculating elements (see Appendix A for details), whose spherical components are

$$r = \frac{a_0(e_0^2 - 1)}{1 + e_0 \cos \varphi(t=0)}, \quad (5)$$

$$\theta = \arccos(z'/r), \quad (6)$$

$$\phi = \arctan(y'/x'), \quad (7)$$

and

$$v_r = v_{x'} \sin \theta \cos \phi + v_{y'} \sin \theta \sin \phi + v_{z'} \cos \theta, \quad (8)$$

$$v_\theta = v_{x'} \cos \theta \cos \phi + v_{y'} \cos \theta \sin \phi - v_{z'} \sin \theta, \quad (9)$$

$$v_\phi = -v_{x'} \sin \phi + v_{y'} \cos \phi, \quad (10)$$

with $\dot{r} = v_r$, $\dot{\theta} = v_\theta/r$ and $\dot{\phi} = v_\phi/(r \sin \theta)$. For the numerical computation, we choose the initial eccentric anomaly to be $\varphi(t=0) = -0.99(\pi - \arctan \sqrt{e_0^2 - 1})$. In all cases we considered, this generates an initially Keplerian orbit.

B. Equation of motion

To account for the post-Newtonian (PN) corrections and environmental effects, we incorporate these as an additional acceleration term \mathbf{F} in the Newtonian equation of the binary system: $\ddot{\mathbf{r}} = -(M/r^2) \mathbf{e}_r + \mathbf{F}$. The explicit, component-wise form is given by

$$\ddot{r} = -\frac{M}{r^2} + r(\dot{\theta})^2 + r \sin^2 \theta (\dot{\phi})^2 + F_r, \quad (11)$$

$$\ddot{\theta} = -\frac{2}{r} \dot{\phi} \dot{r} - 2 \dot{\phi} \dot{\theta} \cot \theta + \frac{F_\theta}{r \sin \theta}, \quad (12)$$

$$\ddot{\phi} = -\frac{2 \dot{r} \dot{\theta}}{r} + (\dot{\phi})^2 \cos \theta \sin \theta + \frac{F_\phi}{r}, \quad (13)$$

with $F_{r,\phi,\theta} = \mathbf{F} \cdot \mathbf{e}_{r,\phi,\theta}$. The relative acceleration due to 1PN and 2.5PN corrections (being the leading-order

¹ If the cumulative dissipation is sufficiently strong, the binary orbit can become bound, resulting in a so called dynamical capture [56]. For the extreme mass-ratio system involving a SMBH, the dynamical captures due to GW damping alone would happen for very small impact parameter (in the unit of M) or incident velocity [57]. We focus instead on the regime of fast hyperbolic encounter (with sufficiently large v_0), during which such capture would not happen.

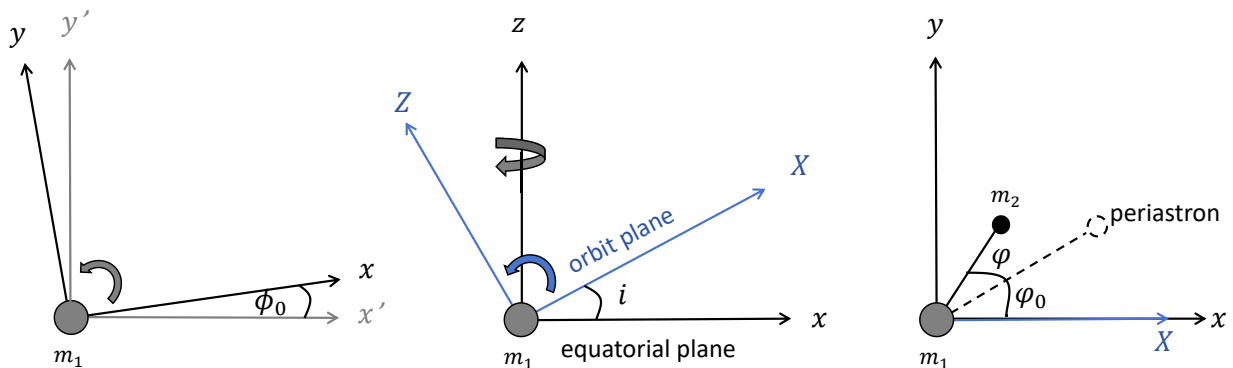


FIG. 2. The definitions of three Cartesian coordinate systems ($x'y'z'$, xyz , XYZ) and the angular osculating orbital elements $\{\phi_0, i, \varphi_0\}$. The central BH lies in the coordinate origin with its spin parallel to the $z' = z$ axis. The osculating orbit lies on the XY plane, with $Y = y$. The $x'y'$ plane is the reference plane.

terms in the conservative and dissipative sectors, respectively) in the harmonic gauge are as follows [59]

$$\frac{\mathbf{F}^{(1\text{PN})}}{M/r^2} = \left[(4 + 2\nu) \frac{M}{r} - (1 + 3\nu) v^2 + \frac{3}{2} \nu (\dot{r})^2 \right] \mathbf{e}_r + (4 - 2\nu) \dot{r} \mathbf{v}, \quad (14)$$

$$\frac{\mathbf{F}^{(2.5\text{PN})}}{M^2/r^3} = \frac{24\nu}{5} \left[\left(v^2 + \frac{17M}{9r} \right) \dot{r} \mathbf{e}_r - \left(\frac{v^2}{3} + \frac{M}{r} \right) \mathbf{v} \right], \quad (15)$$

where $v = |\mathbf{v}|$, $\nu = \mu/M$ is the symmetrical mass ratio and $\mu = m_1 m_2 / M$ is the reduced mass. We do not consider higher-order PN corrections, nor do we employ more refined approaches, such as the post-Minkowskian approximation [60, 61] and geodesic-based method (applicable to extreme mass-ratio binaries) [62]. The higher-order effects are omitted because our primary focus is on the moderately relativistic regime, which is more relevant in the astrophysical scenarios. Once the acceleration \mathbf{F} is specified, we numerically solve Eqs. (11), (12), (13) to determine the orbit $\mathbf{r}(t)$.

III. BLACK HOLE ENVIRONMENTS

From its gravitational interaction with the ambient matter, SMBH in the galaxy center is possibly surrounded by a dense environment, such as the baryonic accretion disk and density spike of particle DM. In this section, we review the physical models of these two types of environments and the resultant gravitational effects on the motion of CO, which include the dissipative dynamical friction and the environmental gravitational potential. In the regime of fast hyperbolic encounter, the latter effect will be more important, since the dissipative force is typically much weaker than the conservative one.

A. DM spike

If the dark matter is composed by massive particles such as weakly-interacting massive particles (WIMPs), the past growth of the central black hole might have enhanced the density of these DM particles at the galaxy center, which can be estimated as follows. We assume the initial DM density profile in the galaxy center is

$$\rho(r) \simeq \rho_0 (r/r_0)^{-\gamma}. \quad (16)$$

If the central BH grows adiabatically through accretion of the ambient DM particles, a density spike would eventually form. The density distribution of this DM spike is given by [63–68]

$$\rho(r) = \rho_{\text{sp}} (1 - 2R_s/r)^3 (r/r_{\text{sp}})^{-\xi}, \quad (17)$$

where $R_s = 2m_1$ is the Schwarzschild radius of the central BH, the parameter $\xi = (9 - 2\gamma)/(4 - \gamma) > 2$ (ξ increases with γ , e.g., for $0 < \gamma < 2$, ξ falls between 2.25 and 2.5), the parameters ρ_{sp} , r_{sp} depend on the SMBH mass m_1 and the initial density distribution (16).

1. Dynamical friction

Due to gravitational scattering with DM particles, the CO experiences a dynamical friction (DF) as it travels in the spike. This DF can be estimated by the classical formula of Chandrasekhar in the Newtonian order² [72]

$$\mathbf{F}^{(\text{DF})} = - \frac{4\pi m_2 \rho_{\text{DM}} \epsilon(v) \ln \Lambda}{v^3} \mathbf{v}, \quad (18)$$

here $\epsilon(v)$ is the fraction of DM particles with velocity $\mathbf{u} = u \mathbf{v}/v$ and $u < v$, for simplicity we shall use the

² We neglect the relativistic correction to the momentum transfer [69, 70] as well as the contribution from DM particles moving faster than CO [71].

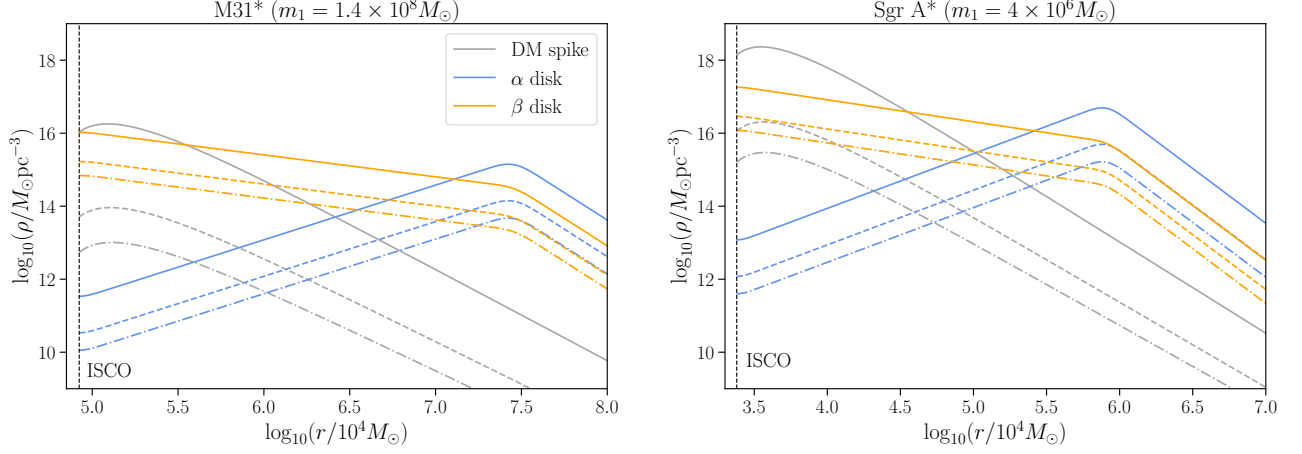


FIG. 3. The mass density distribution of the accretion disk or DM spike around M31* (left panel) and Sgr A* (right panel). The solid, dashed and dot-dashed lines correspond to the viscosity coefficient $\alpha = 0.01, 0.1, 0.3$ for the disk, or the power law index $\gamma = 2, 1, 0$ for the DM spike, respectively.

approximation $\epsilon(v) \approx 1$. $\ln \Lambda$ is the Coulomb logarithm given by [68]

$$\ln \Lambda = \ln \left(\frac{b_{\max}}{b_{\min}} \right) \approx -\frac{1}{2} \ln \left(\frac{m_1}{m_2} \right), \quad (19)$$

where b_{\max} (b_{\min}) is the maximum (minimum) impact parameter of the DM particles relative to CO. E.g., for $m_2 = 10M_\odot$ and $m_1 = 10^8M_\odot$ (10^6M_\odot), this gives $\ln \Lambda \approx 8$ (6).

2. Gravitational potential

The density distribution $\rho(\mathbf{r}) = \rho(r)$ of the considered DM spike is spherically symmetrical, correspondingly the solution of Poisson equation $\nabla^2 \Phi = 4\pi\rho$ is

$$\begin{aligned} \Phi(r) &= -\frac{1}{r} \int_{R_{\text{ISCO}}}^r 4\pi r'^2 \rho_{\text{DM}}(r') dr' \\ &= -4\pi\rho_{\text{sp}} r_{\text{sp}}^\xi \left\{ \left[\frac{8(\xi^2 + 3\xi + 48\xi^{-1} + 20)}{6\xi m_1^{\xi-3} (\xi-1)(\xi-2)(\xi-3)} \right] \right. \\ &\quad \left. + \frac{1}{r^\xi} \left[\frac{r^3}{3-\xi} - \frac{12m_1 r^2}{2-\xi} + \frac{48m_1^2 r}{1-\xi} + \frac{64m_1^3}{\xi} \right] \right\}. \quad (20) \end{aligned}$$

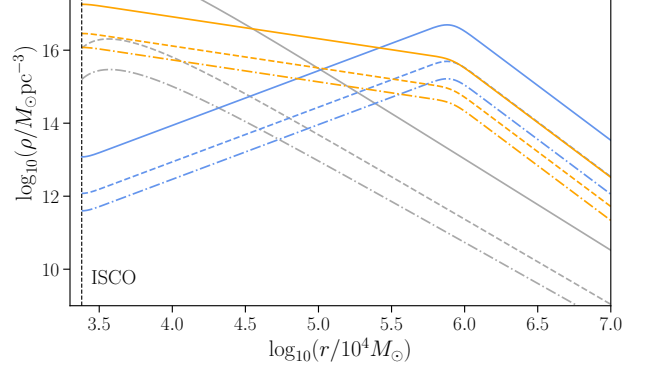
The gravitational acceleration is

$$\mathbf{F}^{(\text{GP})} = -\frac{\partial \Phi}{\partial r} \mathbf{e}_r = F_r^{(\text{GP})} \mathbf{e}_r, \quad (21)$$

where

$$\begin{aligned} F_r^{(\text{GP})} &= 4\pi\rho_{\text{sp}} \times \\ &\left\{ \left[\frac{\xi-2}{\xi-3} r - \frac{12(\xi-1)m_1}{\xi-2} + \frac{48\xi m_1^2}{(\xi-1)r} \right] \left(\frac{r_{\text{sp}}}{r} \right)^\xi - \right. \\ &\left. \left[(\xi+1) \left(\frac{r_{\text{sp}}}{r} \right)^\xi + \frac{6[r_{\text{sp}}/(4m_1)]^\xi}{\xi^3 - 6\xi^2 + 11\xi - 6} \right] \frac{64m_1^3}{\xi r^2} \right\}. \quad (22) \end{aligned}$$

B. Accretion Disk



We consider a stationary accretion disk is geometrically thin, optically thick and radiatively efficient, with opacity primarily determined by the electron scattering [73–75]. The disk temperature is sufficiently high for complete ionization, and the gravitational potential is dominated by the central black hole.

In order to study generic orbits with finite inclination to the disk plane, a three-dimensional model for the gravitational potential of the disk is needed. To construct a reasonable and complete density profile, we divide the disk into the inner ($r < R_Q = 10^3 R_s$) and outer ($r > R_Q$) regions. We use the standard (α and β) disk model [76] with a constant scale height to describe the inner region, and the self-gravitating disk model [77] to describe the outer region (see Appendix B for details). The resultant density profiles for the α and β disks are

$$\begin{aligned} \rho_\beta &= 2.52 \times 10^{-7} \left(\frac{0.3}{\alpha} \right)^{4/5} \left(\frac{10^8 M_\odot}{m_1} \right)^{4/5} \\ &\times \begin{cases} \exp\left(-\frac{Z^2}{2H_{\text{in}}^2}\right) \left(\frac{R}{R_Q} \right)^{-3/5} \text{ g cm}^{-3}, & R \leq R_Q \\ \exp\left(-\frac{Z^2}{2H_{\text{out}}^2}\right) \left(\frac{R}{R_Q} \right)^{-3} \text{ g cm}^{-3}, & R > R_Q \end{cases} \quad (23) \end{aligned}$$

$$\begin{aligned} \rho_\alpha &= 5.51 \times 10^{-8} \left(\frac{0.3}{\alpha} \right) \left(\frac{10^8 M_\odot}{m_1} \right) \\ &\times \begin{cases} \exp\left(-\frac{Z^2}{2H_{\text{in}}^2}\right) \left(\frac{R}{R_Q} \right)^{3/2} \text{ g cm}^{-3}, & R \leq R_Q \\ \exp\left(-\frac{Z^2}{2H_{\text{out}}^2}\right) \left(\frac{R}{R_Q} \right)^{-3} \text{ g cm}^{-3}, & R > R_Q \end{cases} \quad (24) \end{aligned}$$

where α is the viscosity coefficient, $H_{\text{in(out)}}$ the scale height of the inner (outer) region, and (R, Z) the cylindrical coordinates.

1. Dynamical friction

The CO also experiences a dynamical friction in the accretion disk. As an estimation of this effect, we use the Ostriker model of [78], which is derived under the stable supersonic conditions when the CO crosses the disk plane,

$$\mathbf{F}^{(\text{DF})} = -\frac{4\pi m_2 \rho}{v_{\text{rel}}^3} \ln\left(\frac{r_{\text{max}}}{r_{\text{min}}}\right) \mathbf{v}_{\text{rel}}, \quad (25)$$

where \mathbf{v}_{rel} is the velocity of CO relative to the gas, r_{max} and r_{min} are the upper and lower cutoff scales. Specifically we choose [79] $r_{\text{max}} = 2H$ and $r_{\text{min}} = R_{\text{soft}}$, with $R_{\text{soft}} \sim 0.4H$ being the softening radius.

2. Gravitational potential

The density distribution $\rho(\mathbf{r}) = \rho(R, Z)$ of the accretion disk is cylindrically symmetrical, correspondingly the solution to Poisson equation $\nabla^2 \Phi = 4\pi\rho$ is [80]

$$\Phi_{\text{disk}}(R, Z) = -\int_{-\infty}^{\infty} dZ' \int_{R_{\text{min}}}^{R_{\text{max}}} dR' \frac{4R'\rho(R', Z')}{\sqrt{(R+R')^2 + (Z-Z')^2}} K\left(\frac{4RR'}{(R+R')^2 + (Z-Z')^2}\right). \quad (26)$$

The spherical components of the resultant gravitational acceleration are given by

$$F_r^{(\text{GP})}(r, \theta) = \int_{-\infty}^{\infty} dZ' \int_{R_{\text{min}}}^{R_{\text{max}}} dR' \frac{2R'\rho(R', Z')}{r\sqrt{Y_+}} \left[\frac{(R')^2 - r^2 + (Z')^2}{Y_-} E - K \right], \quad (27)$$

$$F_\theta^{(\text{GP})}(r, \theta) = \int_{-\infty}^{\infty} dZ' \int_{R_{\text{min}}}^{R_{\text{max}}} dR' \frac{2R'\rho(R', Z') \cot\theta}{r^2\sqrt{Y_+}} \left\{ \frac{\cot\theta[(R')^2 + r^2 + (Z')^2] - 2Z'r \cos\theta}{Y_-} E - K \right\}, \quad (28)$$

with

$$E = E\left(\frac{4R'r \sin\theta}{(R'+r \sin\theta)^2 + (Z'-r \cos\theta)^2}\right), \quad (29)$$

$$K = K\left(\frac{4R'r \sin\theta}{(R'+r \sin\theta)^2 + (Z'-r \cos\theta)^2}\right), \quad (30)$$

$$Y_\pm = (R')^2 + r^2 + (Z')^2 \pm 2R'r \sin\theta - 2Z'r \cos\theta, \quad (31)$$

where K (E) is the elliptic integral of the first (second) kind. We choose R_{min} to be the ISCO radius and R_{max} to be the outer radius of the disk.

IV. ENVIRONMENTS EFFECTS ON THE ORBITAL EVOLUTION

Using the models of DM spike and accretion disks introduced in the last section, we now examine the orbital evolution of EMRHEs in the vacuum and non-vacuum scenarios. Fig. 4 plots the trajectories of CO projected onto the $x'y'$ and $y'z'$ planes for a given set of parameters. We find that the effect of accretion disk on the variation of scattering angles is stronger than that of the DM spike, and for EMRHEs in the presence of accretion disk, deviations between the vacuum and non-vacuum

trajectories are more distinctive in the case of inclined orbits. We also compare the trajectories with impact parameter $b = 50R_s$ and $b = 500R_s$. The accretion disk typically results in a larger variation of scattering angles at smaller impact parameter, while at near-zero (but finite) inclination, the situation is reversed.

To examine the influence of environmental effects in greater detail, we reconstruct the evolution of osculating elements using the method described in Appendix C. Fig. 5 shows the evolution of orbital eccentricity e and semi-major axis a . The 1PN effect results in an increase (decrease) followed by a later decrease (increase) of the semi-major axis (eccentricity), while the environments typically have opposite effects in the initial and final stages of the orbital evolution. Since the dissipation is relatively weak, there are no visible differences between the initial and final values of eccentricity and semi-major axis, although they show intermediary variations mainly due to the 1PN correction and environmental gravitational potential.

Fig. 6 shows the evolution of angular osculating elements ϕ_0 , φ_0 and i . The non-spherical gravitational potential of the accretion disk induces a precession of the orbital plane (as measured by the angle ϕ_0) and the total precession angle decreases with the inclination; this effect is absent in the case of DM spike. As can be seen, the

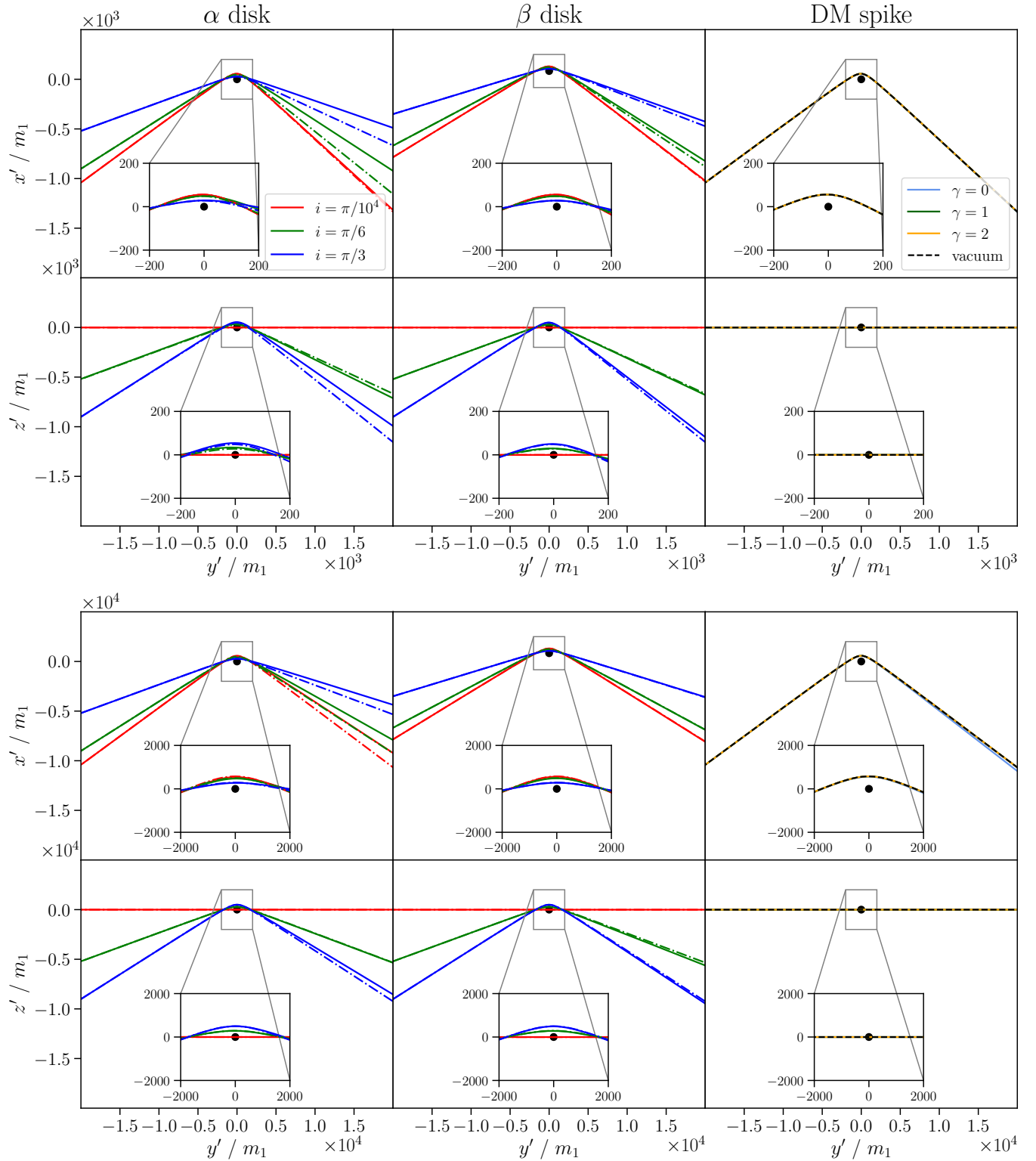


FIG. 4. The projected trajectories of hyperbolic encounters on the $x'y'$ and $y'z'$ planes, with the impact parameter $b = 50R_s$ (upper panel) or $500R_s$ (lower panel), $e_0 = 2.0$, $m_1 = 1.4 \times 10^8 M_\odot$, $m_2 = 10 M_\odot$, $\varphi_0 = 0$, $\phi_0 = 0$ and different initial orbital inclinations. The viscosity coefficient of the accretion disk is set to be $\alpha = 0.01$. The solid (dashed) lines correspond to results in the presence (absence) of environments.

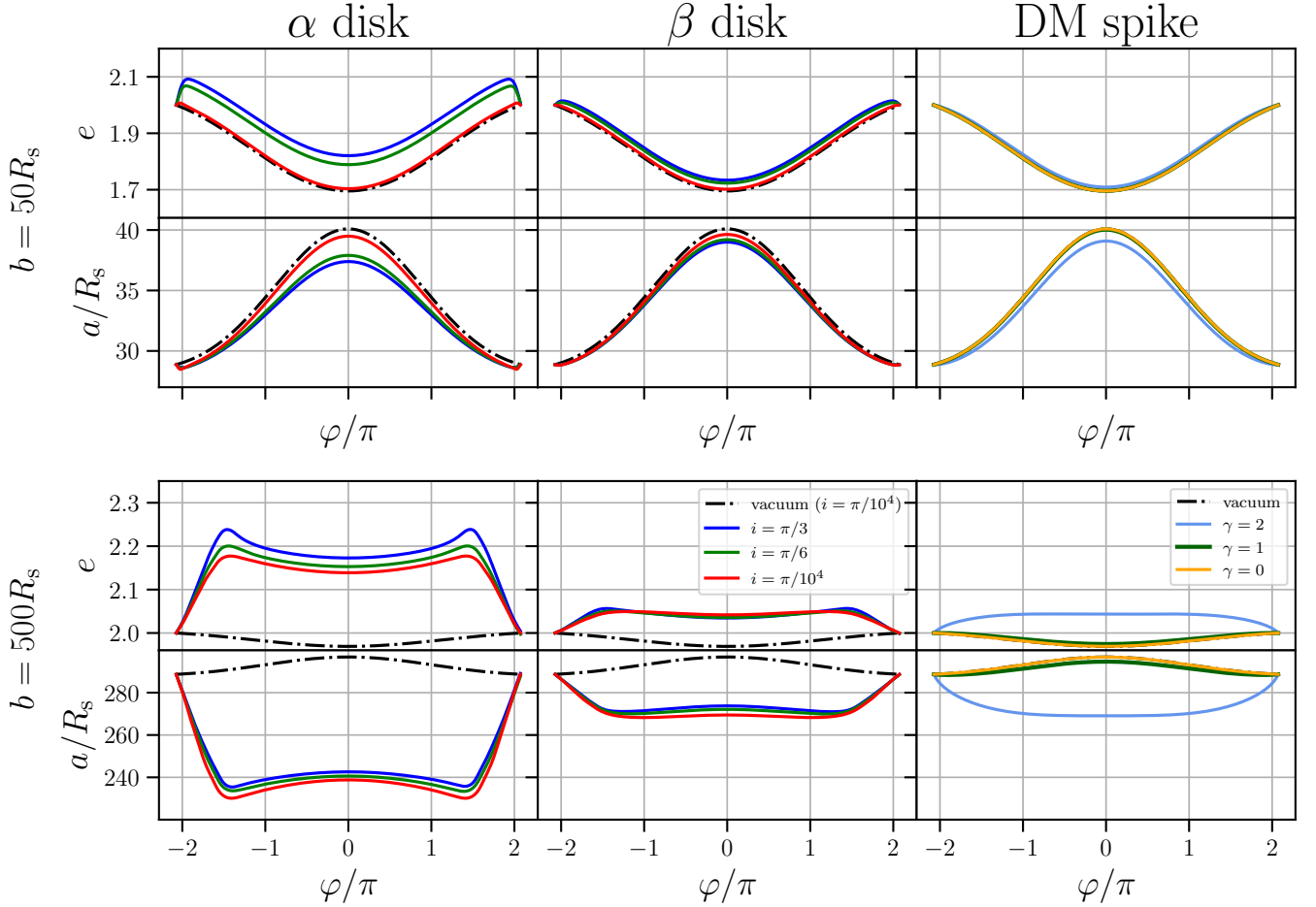


FIG. 5. Evolution of eccentricity e and semi-major axis a during the hyperbolic encounter, with $m_1 = 1.4 \times 10^8 M_\odot$, $m_2 = 10 M_\odot$, $e_0 = 2$ and the impact parameter $b = 50 R_s$ (upper panel) or $500 R_s$ (lower panel). The viscosity coefficient of the accretion disk is set to be $\alpha = 0.01$.

effect of α disk is larger than the β disk under similar conditions, and the DM spike shows only a tiny influence on the orbital precession, unless both the power-law index γ and the impact parameter b are sufficiently large. Increasing the power-law index of DM spike or the viscosity coefficient of accretion disk leads to an overall increase of density, thereby enhancing their environmental effects.

In the case of DM spike, the density profile (17) produces a power-law radial acceleration: $\mathbf{F} = -Ar^{-n}$ for $r \gg R_s$, with $A = 4\pi\rho_{sp}r_{sp}^\xi/(3-\xi)$, $n = \xi - 1$ and $\xi < 3$. The total periastron shift can be estimated using Eq. (C26) (since $\xi > 2$, $n > 1$ is automatically satisfied), as shown with gray dot-dashed line in Fig. 6 for $\gamma = 2$.

V. GRAVITATIONAL WAVES

The modification on the orbital motion of an EMRHE can in principle leave observable imprints in its gravitational wave signals. In this section, we examine the GW waveforms of EMRHEs in the presence of different BH

environments and assess their delectabilities by the LISA detector.

To compute the GW waveforms, we use the leading-order quadrupole formula [81]

$$h_{ij}^{\text{TT}}(t) = \frac{2}{D} \Lambda_{ij,kl}(\mathbf{n}) \ddot{Q}_{kl}(t - D), \quad (32)$$

where D is the distance between the source and detector, \mathbf{n} a unit vector pointing along the propagating direction of GW, and $\Lambda_{ij,kl}(\mathbf{n})$ is the corresponding transverse-traceless projector. The traceless quadrupole moment is

$$Q_{ij} = M_{ij} - \frac{1}{3} \delta_{ij} M_{kk}, \quad M_{ij} = \mu x_i(t) x_j(t). \quad (33)$$

For $\mathbf{n} = (\theta_s, \phi_s)$, the strain tensor can be decomposed into the $+$ and \times modes as

$$h_{ij}^{\text{TT}}(t) = e_{ij}^+ h_+(t) + e_{ij}^\times h_\times(t), \quad (34)$$

with the polarization tensors given by

$$e_{ij}^+ = (\mathbf{e}_\theta)_i (\mathbf{e}_\theta)_j - (\mathbf{e}_\phi)_i (\mathbf{e}_\phi)_j, \quad (35)$$

$$e_{ij}^\times = (\mathbf{e}_\theta)_i (\mathbf{e}_\phi)_j - (\mathbf{e}_\theta)_j (\mathbf{e}_\phi)_i. \quad (36)$$

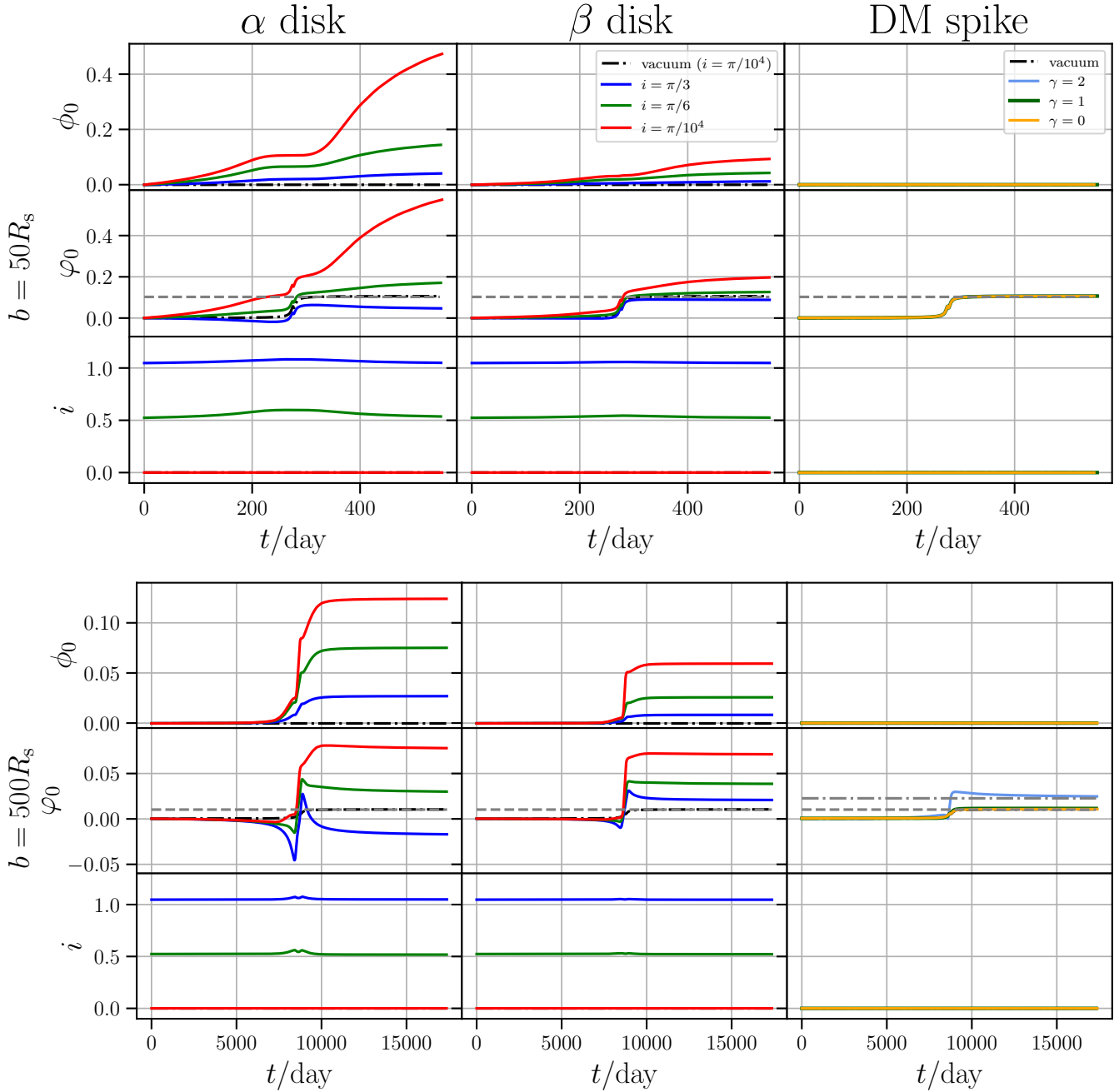


FIG. 6. Evolution of angular osculating orbital elements $\{\phi_0, \varphi_0, i\}$ during the hyperbolic encounter, with impact parameter $b = 50R_s$ (upper panel) or $500R_s$ (lower panel). The setting of other parameters is same with Fig. 5. The horizontal gray dashed line is the analytical approximation to the total periastron shift due to the 1PN correction given by Eq. (C11).

Adding 1PN term (see for example [25]) gives relative correction of $\mathcal{O}(v^2)$ to Eq. (32), as can be checked it is negligible in the cases we considered. The explicit waveforms of the two polarization modes are

$$h_{\times} = \frac{1}{D} [(\ddot{M}_{22} - \ddot{M}_{11}) s_{2\phi_s} c_{\theta_s} + 2\ddot{M}_{12} c_{2\phi_s} c_{\theta_s} + 2\ddot{M}_{13} s_{\phi_s} s_{\theta_s} - 2\ddot{M}_{23} c_{\phi_s} s_{\theta_s}], \quad (37)$$

$$h_{+} = \frac{1}{D} [\ddot{M}_{11} (-s_{\phi_s}^2 + c_{\phi_s}^2 c_{\theta_s}^2) - \ddot{M}_{23} s_{\phi_s} s_{2\theta_s} + \ddot{M}_{22} (-c_{\phi_s}^2 + s_{\phi_s}^2 c_{\theta_s}^2) + \ddot{M}_{33} s_{\theta_s}^2 + \ddot{M}_{12} s_{2\phi_s} (1 + c_{\theta_s}^2) - \ddot{M}_{13} c_{\phi_s} s_{2\theta_s}], \quad (38)$$

where $c_z = \cos z$ and $s_z = \sin z$. Note that these differ from the formulas in [81] since we have used the standard

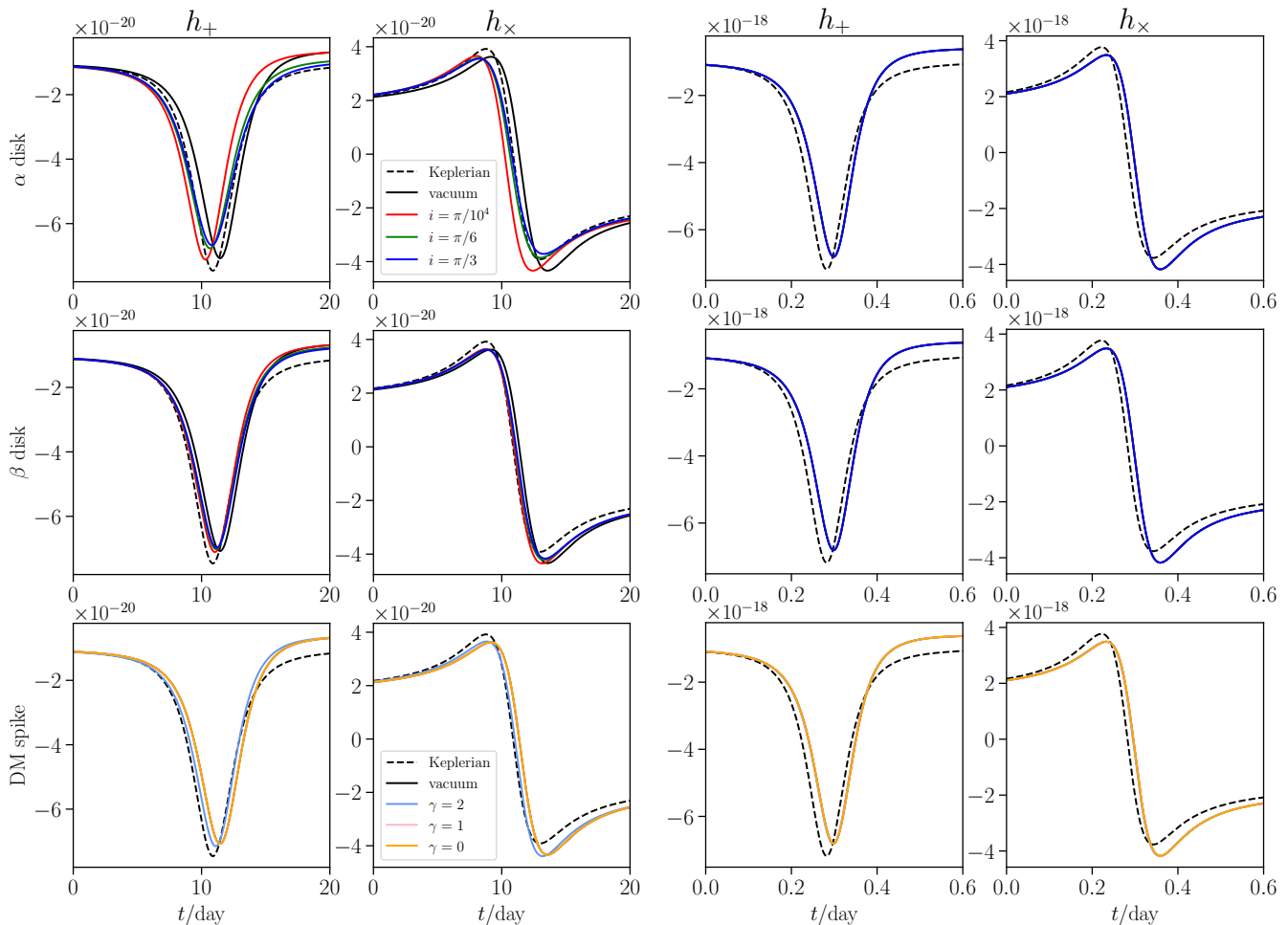


FIG. 7. Time-domain waveforms of EMRHEs around M31* (left two columns) and Sgr A* (right two columns) in different BH environments, with the impact parameter $b = 50R_s$ and initial eccentricity $e_0 = 2$. The mass of the secondary body is $m_2 = 10 M_\odot$. The viscosity coefficient of the accretion disk is set to be $\alpha = 0.01$. In comparison, the waveforms corresponding to the initial osculating Keplerian orbits are shown in dashed lines.

definition of spherical coordinates (θ, ϕ) . To compute the time-domain signal $h(t)$ from $h_{+, \times}(t)$, we adopt the low-frequency response function of LISA as described in [5]. For convenience, we choose the $x'y'z'$ system to be a translation of the ecliptic-based coordinate system used by [5] (in which the source direction is measured), then according to [82], we only need to modify the polarization angle of GW in the Eq. (17) of [5] to

$$\tan \psi = \frac{s_{\bar{\phi}_0 - \phi_s}}{c_{\theta_s}(c_{\bar{\phi}_0} c_{\phi_s} + s_{\bar{\phi}_0} s_{\phi_s}) + s_{\theta_s}/\sqrt{3}}. \quad (39)$$

where the source direction is given by $(\theta_s, \phi_s) = (\pi - \theta_s, \phi_s + \pi)$. The response function also depends on two constant angles $\{\bar{\phi}_0, \bar{\alpha}_0\}$ specifying the orbit of LISA, for simplicity we shall set both to be zero.

Defining $\tilde{h}(f)$ to be the Fourier transform of $h(t)$, the optimal signal-to-noise ratio (SNR) of a matched filtering

is given by [83]

$$\text{SNR}^2 = \int d \ln f \left(\frac{h_c}{\sqrt{f S_n}} \right)^2, \quad (40)$$

where $S_n(f)$ is the one-sided noise power spectral density, and $h_c(f) = 2f\tilde{h}(f)$ is the characteristic strain.

For concreteness, we choose \mathbf{n} to be normal to the initial orbital plane (i.e., parallel to \mathbf{e}_z), such that the waveforms for different orbital inclinations are same in the vacuum case. In Fig. 7, we show the time-domain waveforms of EMRHEs around M31* [84, 85] and Sgr A* [86] (the corresponding density profiles of accretion disk and DM spike are plotted in Fig. 3), using the same parameters as Fig. 4. As can be seen, the modifications to the orbital evolution are reflected in the time-domain waveforms as variations in the shape, peak position and the amount of GW memory $\Delta h = h(\infty) - h(-\infty)$.

In the case of accretion disk, the peak shift is most pronounced when the inclination angle is small, in which case

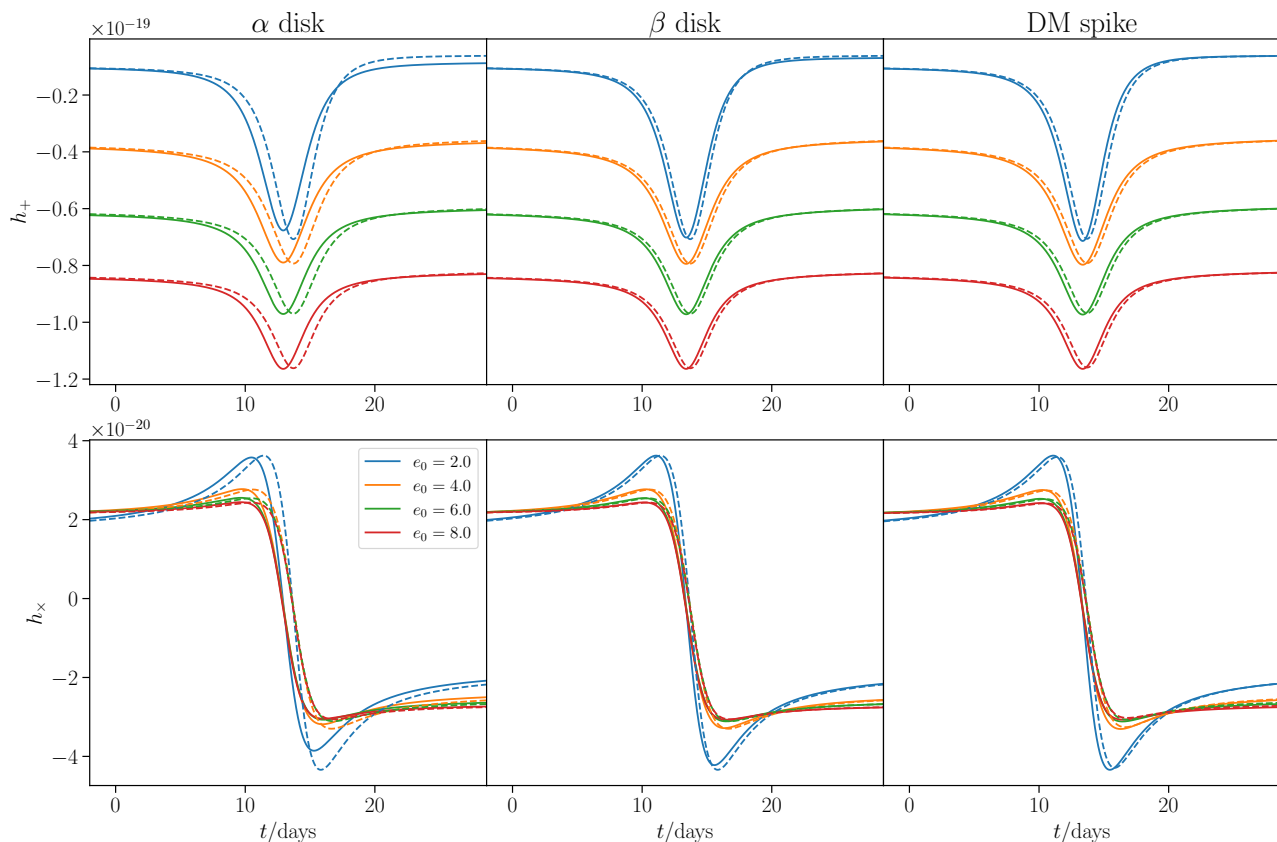


FIG. 8. Time-domain waveforms of EMRHEs around M31* with the impact parameter $b = 50R_s$, orbital inclination $i_0 = \pi/6$ and different initial eccentricity e_0 . The viscosity coefficient of the accretion disk is set to be $\alpha = 0.01$ and the DM spike power law index is set to be $\gamma = 2$. The solid (dashed) lines correspond to results in the presence (absence) of environments.

the orbit remains close to the disk plane for a relatively long time and the orbital evolution is affected by the gravitational potential of the disk at an early stage. As the orbital inclination decreases, the waveform peak of + mode becomes steeper, accompanied by an enhancement in its GW memory. The difference between vacuum and non-vacuum waveforms is most visible in the case of α disk; in the case of DM spike, the difference increases with the power-law index γ . Given same CO mass, impact parameter and initial eccentricity, the vacuum and non-vacuum waveforms are harder to distinguish for events around Sgr A* compared to those around M31*. We also compare the time-domain waveforms of EMRHE events with varying initial eccentricities in Fig. 8. As can be seen, decreasing the orbital eccentricity generally increase the peak amplitude as well as the difference between vacuum and non-vacuum waveforms.

Taking into account the response function of LISA detector, we compute the optimal SNR for a set of EMRHEs around Sgr A* and M31* in the vacuum case, as shown in Fig. 9. For given initial eccentricity, the square of maximum velocity reached during the encounter can be estimated by the Keplerian value $v_{\max}^2 \approx [(e_0 + 1)/(e_0 - 1)](M/a_0)$ (as indicated by the red lines), which remains small throughout the depicted parameter space, justify-

ing the use of 1PN approximation. For each event, the sampling time range of the waveform corresponds to the orbital evolution from $\varphi = \varphi(t = 0)$ to $\varphi = -\varphi(t = 0)$. In the case of Sgr A* source, the SNR at LISA reaches $10^2 \sim 10^3$ when the impact parameter is about several tens of Schwarzschild radii, a similar event near M31* can have a SNR around 10. Such events are likely to be detectable and with an estimated event rate about 0.8 per year [7], making them potential targets for the space-based gravitational wave detectors.

As concrete examples, we plot the characteristic strains of two EMRHE events in Fig. 10. For the M31* source (lower line), the peak in the frequency spectrum shows clear modifications due to environmental effects. These peaks, however, are below the sensitivity curve of LISA. The spectral peak of the Sgr A* event (upper line) is more detectable, but in which the imprints of environment is much less visible. Interestingly, both events produce detectable flat high-frequency spectral tails (a manifestation of the GW memory), we postpone the detailed study of this intriguing GW signature to a future work.

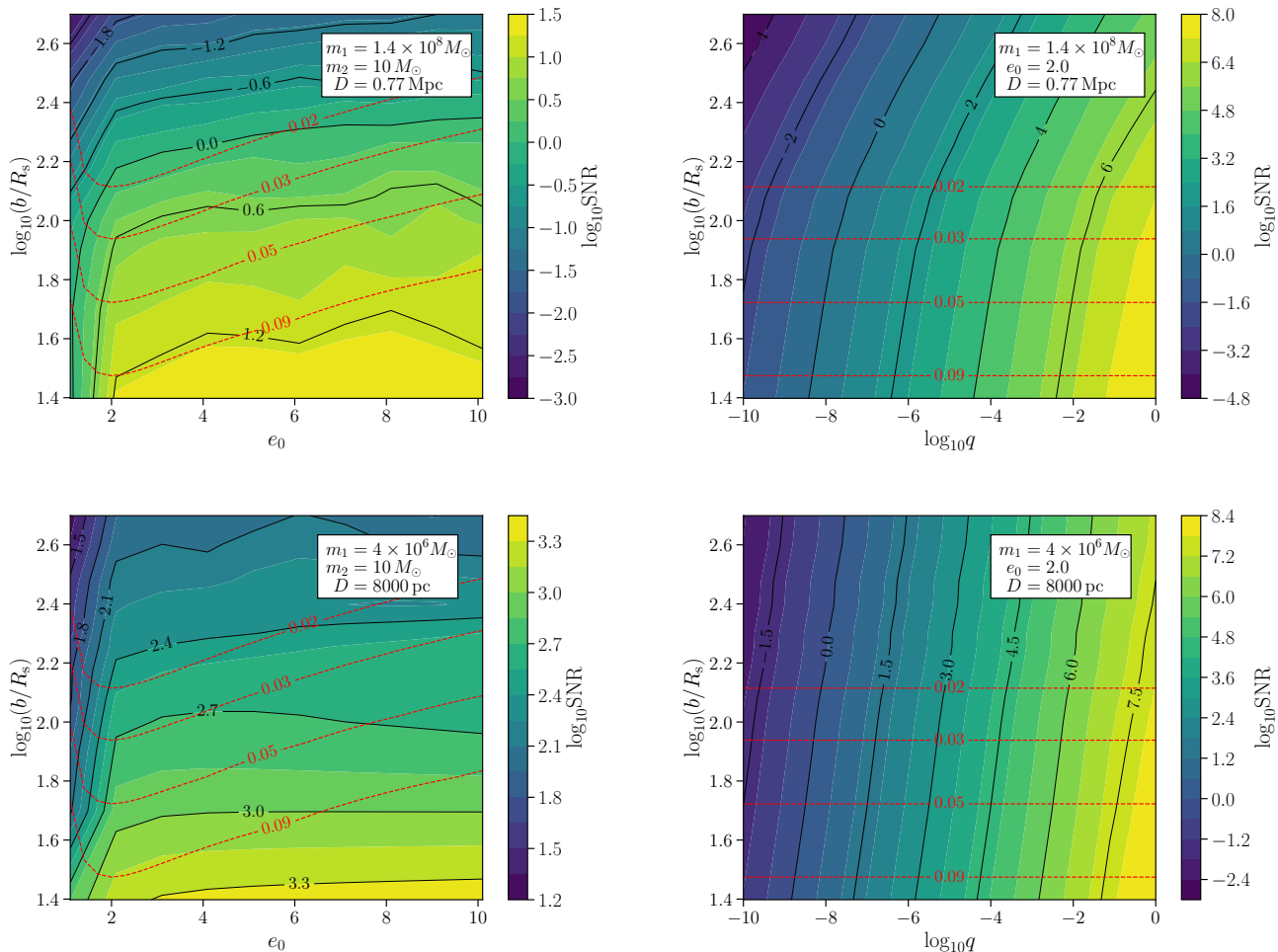


FIG. 9. The SNR of vacuum EMRHEs around M31* (upper row) and Sgr A* (lower row) at LISA, as functions of initial eccentricity e_0 (left column) or mass ratio q (right column) and the impact parameter b . The contours of $v_{\max}^2 \approx [(e_0 + 1)/(e_0 - 1)](M/a_0)$ are shown in red lines.

VI. CONCLUSION AND DISCUSSION

We have investigated the orbital evolution and GW waveforms of EMRHEs near a supermassive black hole surrounded by accretion disk or a DM spike. Our computation incorporates the conservative and dissipative environmental effects as well as the leading PN corrections. For each type of environment, the evolution of osculating orbital elements is tracked and analyzed. In the case of accretion disk, we construct a three-dimensional model for its gravitational potential, which allows us to examine the full range of initial conditions for the hyperbolic scattering. We find that the primary influence of a black hole environment on the hyperbolic encounter comes from its gravitational potential rather than the dissipative effects such as dynamical friction. Additionally, the impact of DM spike on the orbital evolution is found to be typically much smaller than that of accretion disk, especially for an orbit with finite inclination.

We also demonstrate the detectability of such extreme mass-ratio encounters and the discriminability of BH environments in the waveforms. We find that events which show clear modifications of waveforms due to the presence of environments are typically below the sensitivity of near future LISA-like detectors. On the other hand, for detectable events the imprints of environments on GW waveform are small, thus requiring more sensitive detectors or more advanced analysis methods to distinguish them.

As possible extensions of the present work, other types of BH environments can be considered, such as the non-relativistic cloud of ultralight bosons³, for which the environmental gravitational potential is fixed by the wavefunction of the cloud [88]. Besides the environmental ef-

³ See [87] for an estimation of the energy dissipation of hyperbolic orbit in the scalar [211] cloud.

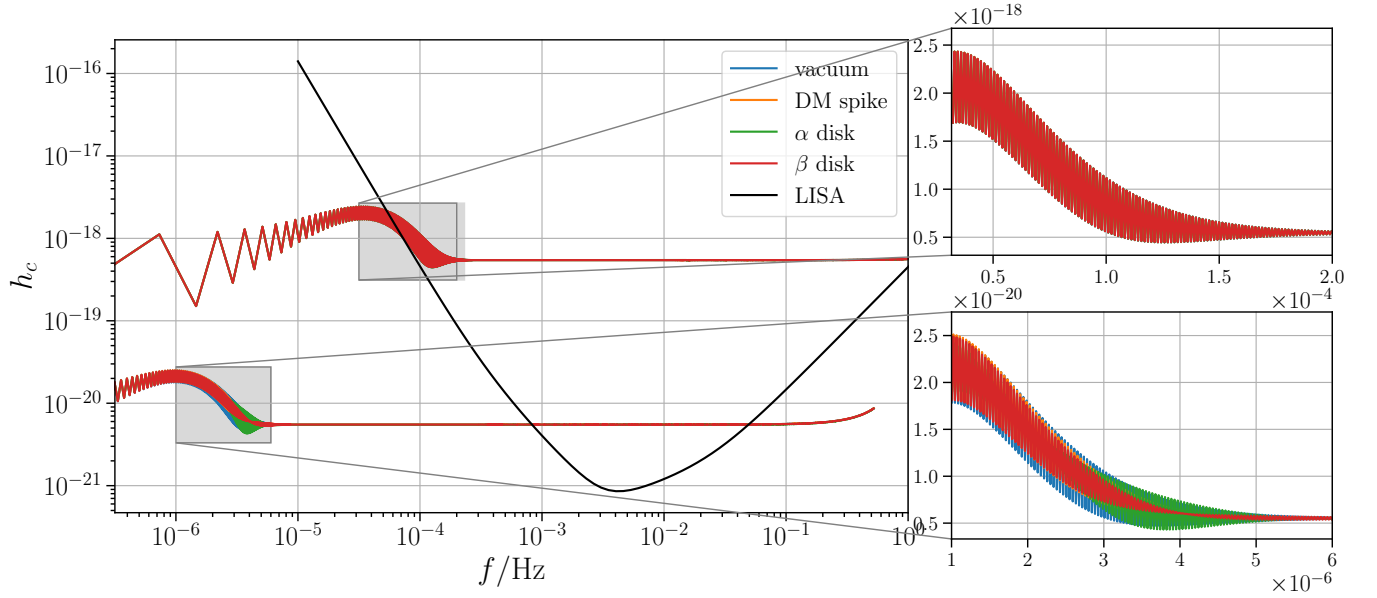


FIG. 10. The GW frequency spectrum of two EMRHE events in different BH environments, with the central SMBH being Sgr A* (upper curve) and M31* (lower curve), respectively. The right panels show the zoomed-in views of the spectral peaks. The initial condition of both events is $b = 50R_s$ and $e_0 = 2$, with the viscosity coefficient of the accretion disk set to be $\alpha = 0.01$ and the power law index of DM spike set to be $\gamma = 2$.

fects, modifications to the intrinsic binary dynamics (e.g., due to the presence of scalar or vector charges [36, 89]) can also be examined. Going beyond the Newtonian regime, a fully relativistic description of the binary as well as the environments [53] is needed for an accurate modeling of such systems.

ACKNOWLEDGEMENT

This work is supported by the National Key Research and Development Program of China (No. 2021YFC2201901), the National Natural Science Foundation of China (No. 12347103) and the Fundamental Research Funds for the Central Universities.

Appendix A: Initial condition and reconstruction of osculating elements

Given the initial osculating elements $\{a, e, \varphi_0, \phi_0, i\}$ and true anomaly φ , the initial orbital radius is

$$r = \frac{a(e^2 - 1)}{1 + e \cos \varphi}, \quad (\text{A1})$$

with the Cartesian components of position $\mathbf{r} = x'\mathbf{e}_{x'} + y'\mathbf{e}_{y'} + z'\mathbf{e}_{z'}$ and velocity $\mathbf{v} = v_{x'}\mathbf{e}_{x'} + v_{y'}\mathbf{e}_{y'} + v_{z'}\mathbf{e}_{z'}$ in

the fixed $x'y'z'$ coordinate system (see Fig. 2) given by

$$\begin{aligned} \frac{x'}{r} &= \cos i \cos \phi_0 \cos(\varphi + \varphi_0) - \sin \phi_0 \sin(\varphi + \varphi_0), \\ \frac{y'}{r} &= \cos i \sin \phi_0 \cos(\varphi + \varphi_0) + \cos \phi_0 \sin(\varphi + \varphi_0), \\ \frac{z'}{r} &= \sin i \cos(\varphi + \varphi_0), \end{aligned} \quad (\text{A2})$$

and

$$\begin{aligned} v_{x'} &= \sqrt{\frac{M}{a(e^2 - 1)}} \left\{ -\sin \phi_0 [e \cos \varphi_0 + \cos(\varphi + \varphi_0)] \right. \\ &\quad \left. - \cos i \cos \phi_0 [e \sin \varphi_0 + \sin(\varphi + \varphi_0)] \right\}, \\ v_{y'} &= \sqrt{\frac{M}{a(e^2 - 1)}} \left\{ \cos \phi_0 [e \cos \varphi_0 + \cos(\varphi + \varphi_0)] \right. \\ &\quad \left. - \cos i \sin \phi_0 [e \sin \varphi_0 + \sin(\varphi + \varphi_0)] \right\}, \\ v_{z'} &= -\sqrt{\frac{M}{a(e^2 - 1)}} \sin i [e \sin \varphi_0 + \sin(\varphi + \varphi_0)]. \end{aligned} \quad (\text{A3})$$

Once a trajectory $\mathbf{r}(t)$ is computed, the osculating orbital elements can be obtained as follows [90]. Introducing the vectors of angular momentum, ascending node

disk type	b	ϵ	κ	μ	X_{H}	l_{E}
α	0	0.1	$0.349 \text{ cm}^2 \text{ g}^{-1}$	1.756	0.75	0.1
β	1	0.1	$0.349 \text{ cm}^2 \text{ g}^{-1}$	1.756	0.75	0.1

TABLE I. The choices for various parameters in the disk model. ϵ is the radiative efficiency of the disk and κ is the gas opacity.

and eccentricity:

$$\mathbf{L} = \mathbf{e}_r \times \mathbf{v}, \quad (\text{A4})$$

$$\mathbf{N} = \mathbf{e}_{z'} \times \mathbf{L}, \quad (\text{A5})$$

$$\mathbf{e} = \frac{1}{M} \left[\left(v^2 - \frac{M}{r} \right) \mathbf{e}_r - (\mathbf{e}_r \cdot \mathbf{v}) \mathbf{v} \right], \quad (\text{A6})$$

we have

$$a = \left(\frac{2}{r} - \frac{v^2}{M} \right)^{-1}, \quad (\text{A7})$$

$$e = |\mathbf{e}|, \quad (\text{A8})$$

$$i = \arccos \left(\frac{\mathbf{L} \cdot \mathbf{e}_{z'}}{|\mathbf{L}|} \right), \quad (\text{A9})$$

$$\varphi_0 = \arccos \left(\frac{\mathbf{N} \cdot \mathbf{e}}{|\mathbf{N}|e} \right) - \frac{\pi}{2}, \quad (\text{A10})$$

$$\phi_0 = \arccos \left(\frac{\mathbf{N} \cdot \mathbf{e}_{x'}}{|\mathbf{N}|} \right) - \frac{\pi}{2}, \quad (\text{A11})$$

$$\varphi = \arccos \left(\frac{\mathbf{e} \cdot \mathbf{e}_r}{er} \right). \quad (\text{A12})$$

Appendix B: Density distribution of accretion disk

We consider a standard disk [91] with the surface mass density given by [76]

$$\Sigma_0 = 2.56 \times 10^5 (\alpha_{0.3} \beta^{b-1})^{-4/5} l_{\text{E}}^{3/5} \epsilon_{0.1}^{-3/5} \hat{\kappa}^{-1/5} \mu^{4/5} \times \left(\frac{m_1}{10^8 M_{\odot}} \right)^{1/5} \left(\frac{R}{R_{\text{Q}}} \right)^{-3/5} \text{ g cm}^{-2}, \quad (\text{B1})$$

where $\hat{\kappa}$ is the opacity (in the unit of electron scattering opacity of the ionized hydrogen, $0.4 \text{ cm}^2 \text{ g}^{-1}$), μ the average molecular mass (in the unit of atomic mass of hydrogen), $\alpha_{0.3} = \alpha/0.3$ the Shakura-Sunyaev viscosity coefficient (with $\alpha = 0.01 \sim 0.3$), $\beta = p_{\text{gas}}/p$ and $\epsilon = L/\dot{M}c^2 = 0.1 \epsilon_{0.1}$ the radiative efficiency of the disk. The parameter b determines whether the viscosity depends on the total pressure (called β disk) or only the gas pressure (called α disk).

For the parameter β , we use [76]

$$\frac{\beta^{(1/2)+(b-1)/10}}{1-\beta} \approx 0.311 \alpha_{0.3}^{-1/10} \hat{\kappa}^{-9/10} \mu^{-2/5} (\epsilon_{0.1}/l_{\text{E}})^{4/5} \times \left(\frac{m_1}{10^8 M_{\odot}} \right)^{-1/10} \left(\frac{R}{R_{\text{Q}}} \right)^{21/20}, \quad (\text{B2})$$

here $l_{\text{E}} = \dot{m}_1/\dot{m}_{\text{Edd}}$ is the ratio of the central BH's mass accretion rate to the Eddington rate, typically l_{E} is around $0.1 \sim 1$ [92]. For simplicity, we fix the disk parameters according to Table I, leaving only a single free parameter α .

Within the gravitational stability radius R_{Q} of the disk ($r < R_{\text{Q}}$), radiative pressure dominates, Eq. (B2) becomes

$$\beta^{(1/2)+(b-1)/10} \approx 0.281 \alpha_{0.3}^{-1/10} l_{\text{E}}^{-4/5} \left(\frac{m_1}{10^8 M_{\odot}} \right)^{-1/10} \times \left(\frac{R}{R_{\text{Q}}} \right)^{21/20}. \quad (\text{B3})$$

For the β disk, we assume that $\beta \ll 1$, $b = 1$, $R \leq 10^3 R_{\text{s}}$, then Eq. (B1) gives the density distribution

$$\rho_{\beta} = \frac{\Omega \Sigma_{\beta}(R)}{2c_{\text{s}}} \exp \left(-\frac{Z^2}{2H_{\text{in}}^2} \right) \approx 7.98 \times 10^{-10} \left(\frac{\alpha}{0.3} \right)^{-4/5} l_{\text{E}}^{-2/5} \exp \left(-\frac{Z^2}{2H_{\text{in}}^2} \right) \times \left(\frac{m_1}{10^8 M_{\odot}} \right)^{-4/5} \left(\frac{R}{R_{\text{Q}}} \right)^{-3/5} \text{ g cm}^{-3}, \quad (\text{B4})$$

the cylindrical coordinates (R, Z) are related to the spherical coordinates (r, θ) via $R = r \sin \theta$ and $Z = r \cos \theta$. For the α disk ($\beta \ll 1$, $b = 0$, $R \leq 10^3 R_{\text{s}}$), we obtain

$$\rho_{\alpha} = \frac{\Omega \Sigma_{\alpha}(R)}{2c_{\text{s}}} \exp \left(-\frac{Z^2}{2H_{\text{in}}^2} \right) \approx 5.51 \times 10^{-11} \left(\frac{\alpha}{0.3} \right)^{-1} l_{\text{E}}^{-2} \exp \left(-\frac{Z^2}{2H_{\text{in}}^2} \right) \times \left(\frac{m_1}{10^8 M_{\odot}} \right)^{-1} \left(\frac{R}{R_{\text{Q}}} \right)^{3/2} \text{ g cm}^{-3}. \quad (\text{B5})$$

The scale height of the inner disk can be estimated as [76]

$$H_{\text{in}} = \frac{c_{\text{s}}}{\Omega} \approx 8.725 l_{\text{E}} R_{\text{s}}, \quad (\text{B6})$$

where $c_{\text{s}} = \sqrt{p/\rho}$ is the isothermal sound speed and $\Omega = \sqrt{m_1/R^3}$ is the Keplerian orbital frequency.

For $R \geq R_{\text{Q}}$, we adopt the disk model of [93], the density is given by

$$\rho(R, Z) = \rho(R_{\text{Q}}, 0) \left(\frac{R_{\text{Q}}}{R} \right)^3 \exp \left(-\frac{Z^2}{2H_{\text{out}}^2} \right), \quad (\text{B7})$$

with $H_{\text{out}} \approx (R/R_{\text{Q}})^{3/2} H_{\text{in}}$ being the scale height of the outer disk.

Appendix C: Analytical approximation to the variations of osculating orbital elements

In this appendix, we derive analytical approximations to the changes of osculating elements during a hyperbolic encounter due to the leading PN corrections. To the best of our knowledge, these have not been derived previously. Recall that a Keplerian hyperbolic orbit can be parameterized by six orbital elements $\{a, e, \varphi_0, \phi_0, i, t_0\}$, with

$$r = \frac{a(e^2 - 1)}{1 + e \cos \varphi} = a(e \cosh \xi - 1), \quad \mathcal{M} = e \sinh \xi - \xi = \Omega(t - t_0), \quad (\text{C1})$$

where the true anomaly $\varphi \in [-(\pi - \arctan \sqrt{e^2 - 1}), \pi - \arctan \sqrt{e^2 - 1}]$, the eccentric anomaly $\xi \in [-\infty, \infty]$, \mathcal{M} the mean anomaly, t_0 the periastron-crossing time, $\Omega = \sqrt{M/a^3}$, and the impact parameter $b = a\sqrt{e^2 - 1}$. The relation between φ and ξ is given by

$$\varphi = 2 \operatorname{arctanh} \left[\left(\frac{1+e}{e-1} \right)^{1/2} \tanh \frac{\xi}{2} \right], \quad \cos \varphi = \frac{e - \cosh \xi}{e \cosh \xi - 1}, \quad \sin \varphi = \frac{\sqrt{e^2 - 1} \sinh \xi}{e \cosh \xi - 1}. \quad (\text{C2})$$

The conserved energy and angular momentum are $E = v^2/2 - M/r = M/(2a)$ and $\mathbf{h} = \mathbf{r} \times \mathbf{v} = \sqrt{(e^2 - 1)aM} \mathbf{e}_Z$.

In the presence of additional acceleration $\mathbf{F} = F_r \mathbf{e}_r + F_\varphi \mathbf{e}_\varphi + F_Z \mathbf{e}_Z$, where $\mathbf{e}_\varphi = \mathbf{e}_Z \times \mathbf{e}_r$, the complete set of Gaussian perturbation equation for the osculating hyperbolic orbit reads

$$\frac{\dot{a}}{a} = -\frac{2}{\Omega} \left(\frac{e \sin \varphi}{a\sqrt{e^2 - 1}} F_r + \frac{\sqrt{e^2 - 1}}{r} F_\varphi \right), \quad (\text{C3})$$

$$\dot{e} = \frac{\sqrt{e^2 - 1}}{a\Omega} [(\cos \varphi + \cosh \xi) F_\varphi + \sin \varphi F_r], \quad (\text{C4})$$

$$\dot{\varphi}_0 = \frac{\sqrt{e^2 - 1}}{ae\Omega} \left[\left(1 + \frac{ar}{b^2} \right) \sin \varphi F_\varphi - \cos \varphi F_r \right] - \cos i \dot{\phi}_0, \quad (\text{C5})$$

$$\dot{\phi}_0 = \frac{r \sin(\varphi + \varphi_0 + \pi/2) F_Z}{a^2 \Omega \sqrt{e^2 - 1} \sin i}, \quad (\text{C6})$$

$$\dot{i} = \frac{r \cos(\varphi + \varphi_0 + \pi/2) F_Z}{a^2 \Omega \sqrt{e^2 - 1}}, \quad (\text{C7})$$

$$\dot{\epsilon} = (1 - e \cosh \xi) \frac{a \cosh \xi \dot{e} - (1 - e \cosh \xi) \dot{a}}{ae \sinh \xi} + \sinh \xi \dot{e}. \quad (\text{C8})$$

Here ϵ is the compensated mean anomaly defined by $\epsilon = \mathcal{M} - \int_0^t dt' \Omega(t')$ such that $\dot{\epsilon} = \dot{\mathcal{M}} - \Omega$.

We consider the 1PN and 2.5PN acceleration given by Eq. (14) and (15), as well as a relative acceleration due to a fixed spin $\mathbf{J} = J \mathbf{e}_z$ of the primary body [94]

$$\mathbf{F}^{(\text{spin})} = (1+q)^2 \frac{1 + \sqrt{1-4\nu}}{4r^3} \{ 12\mathbf{e}_r [(\mathbf{e}_r \times \mathbf{v}) \cdot \mathbf{J}] - (7 + \sqrt{1-4\nu}) \mathbf{v} \times \mathbf{J} + (9 + 3\sqrt{1-4\nu}) \dot{r} (\mathbf{e}_r \times \mathbf{J}) \}, \quad (\text{C9})$$

and the relative acceleration due to a quadrupolar Newtonian potential of the primary body (with its symmetry axis parallel to \mathbf{e}_z),

$$\mathbf{F}^{(\text{quad})} = -\nabla \Phi_{\text{quad}}, \quad \Phi_{\text{quad}} = \left(\frac{M}{m_1} \right) \frac{Q}{r^3} \frac{1 - 3 \cos^2 \theta}{2}. \quad (\text{C10})$$

This can also be applied to the spin-induced quadrupole moment of Kerr BH (with $J = m_1^2 \chi$) [95] $Q = -m_1^3 \chi^2$. We assume a fixed spin or symmetry axis \mathbf{e}_z for the primary body and neglect the spin of the secondary body, which is a reasonable approximation if the mass ratio $q = m_2/m_1$ is sufficiently small.

The change of an orbital element \mathcal{X} after the encounter is approximately given by $\Delta \mathcal{X} \approx \int_{-\infty}^{\infty} dt \dot{\mathcal{X}}$, with the osculating elements involved in $\dot{\mathcal{X}}$ fixed to their initial values. The results obtained from the Gaussian perturbation

equation are

$$\frac{(\Delta\varphi_0)_{1\text{PN}}}{\frac{M}{a}} = \frac{\sqrt{e^2-1} [(5\nu+2)e^2 - 5\nu + 4] + 12e^2 \arctan \frac{e+1}{\sqrt{e^2-1}}}{e^2(e^2-1)}, \quad (\text{C11})$$

$$\begin{aligned} \frac{(\Delta\varphi_0)_{\text{spin}}}{\frac{(1+q)^2 J \cos i}{e^2(e^2-1)^2(a^3 M)^{1/2}}} &= e^2 (2\nu \cos 2\varphi_0 + \nu + 2\sqrt{1-4\nu} + 2) + 6e^2 g(e) \sqrt{e^2-1} (\nu - 2\sqrt{1-4\nu} - 2) \\ &\quad + e^4 (-\nu \cos 2\varphi_0 + \nu - 4\sqrt{1-4\nu} - 4) - \nu \cos 2\varphi_0 - 2\nu + 2\sqrt{1-4\nu} + 2, \end{aligned} \quad (\text{C12})$$

$$\begin{aligned} \frac{(\Delta\phi_0)_{\text{spin}}}{\frac{(1+q)^2 J}{e^2(e^2-1)^2(a^3 M)^{1/2}}} &= e^2 (-2\nu \cos 2\varphi_0 + \nu - 2\sqrt{1-4\nu} - 2) + 2e^2 g(e) \sqrt{e^2-1} (-\nu + 2 + 2\sqrt{1-4\nu}) \\ &\quad + e^4 (\nu \cos 2\varphi_0 - \nu + 2\sqrt{1-4\nu} + 2) + \nu \cos 2\varphi_0, \end{aligned} \quad (\text{C13})$$

$$\frac{(\Delta i)_{\text{spin}}}{\frac{(1+q)^2 J}{(a^3 M)^{1/2}}} = -\frac{\nu \sin 2\varphi_0}{e^2} \sin i, \quad (\text{C14})$$

$$\frac{(\Delta\varphi_0)_{\text{quad}}}{\frac{Q}{a^2 m_1}} = \frac{2(1-e^2) [(2e^2-1) \cos 2i + 1] \cos 2\varphi_0 - e^2 [3(4e^2+1) \cos 2i + 8e^2 + 1]}{4e^4(e^2-1)^{3/2}} - g(e) \frac{15 \cos 2i + 9}{2(e^2-1)^2}, \quad (\text{C15})$$

$$\frac{(\Delta\phi_0)_{\text{quad}}}{\frac{Q}{a^2 m_1}} = \frac{\sqrt{e^2-1} [(e^2-1) \cos 2\varphi_0 + 3e^2] + 6e^2 g(e)}{e^2(e^2-1)^2} \cos i, \quad (\text{C16})$$

$$\frac{(\Delta i)_{\text{quad}}}{\frac{Q}{a^2 m_1}} = -\frac{\sin 2\varphi_0}{2e^2 \sqrt{e^2-1}} \sin 2i, \quad (\text{C17})$$

$$\frac{\left(\frac{\Delta e}{e}\right)_{2.5\text{PN}}}{\left(\frac{M}{a}\right)^{5/2}} = -\frac{2\nu}{45(e^2-1)^2} \left[1069 + 72e^2 + \frac{134}{e^2} + \frac{6(121e^2 + 304)g(e)}{\sqrt{e^2-1}} \right], \quad (\text{C18})$$

$$\frac{\left(\frac{\Delta a}{a}\right)_{2.5\text{PN}}}{\left(\frac{M}{a}\right)^{5/2}} = \frac{4\nu}{45(e^2-1)^4} \left[-602 + 673e^4 - 71e^2 + 6(37e^4 + 292e^2 + 96)g(e)\sqrt{e^2-1} \right], \quad (\text{C19})$$

where $g(e) = \arctan \frac{e-1}{\sqrt{e^2-1}} + \arcsin \frac{1}{e}$. $\mathbf{F}^{(1\text{PN})}$, $\mathbf{F}^{(\text{spin})}$ and $\mathbf{F}^{(\text{quad})}$ do not contribute to Δe and Δa . These are compared with numerical results in Fig. 11, showing good agreements in all cases. In principle one can add corrections of higher PN order, but also a higher-order perturbative treatment of the Gaussian perturbation equation would be needed to handle these properly (similar to the case of bound-orbit case [96]), and in the leading-order approximation considered here they are negligible. Note that a 1PN-exact quasi-Keplerian parametrization of the unbound orbit was derived in [97] (which can be obtained from the parametrization of bound orbit by the analytical continuation: $\xi \rightarrow i\xi$, $a \rightarrow -a$, $\Omega \rightarrow -i\Omega$ and $\sqrt{1-e^2} \rightarrow i\sqrt{e^2-1}$), when the 1PN conserved quantities are evaluated using the full initial conditions corresponding to the ingoing Keplerian osculating orbit with elements $\{a, e\}$ (without making the $r \rightarrow \infty$ approximation), it gives a total periastron shift which is generally more accurate than Eq. (C11) but the relative difference is below $\mathcal{O}(M/a)$. The results above can be used to derive the leading relativistic corrections to the magnitude of linear memory in the GW waveform of a hyperbolic encounter (which is fixed by the initial and final osculating elements). They can also be used to improve the estimation of relativistic dynamical friction [70, 98].

Here we also present the periastron shift for a more generically parameterized 1PN binary Lagrangian, allowing deviations from the standard vacuum GR:

$$\begin{aligned} L &= \frac{m_1 v_1^2 + m_2 v_2^2}{2} + \frac{m_1 v_1^4 + m_2 v_2^4}{8} + \frac{m_1 m_2}{r} A' - \frac{m_1 m_2 (m_1 + m_2)}{2r^2} B' \\ &\quad + \frac{m_1 m_2}{2r} [3(v_1^2 + v_2^2) C' - 7\mathbf{v}_1 \cdot \mathbf{v}_2 D'] - \frac{m_1 m_2}{2r} \{(\mathbf{v}_1 \cdot \mathbf{e}_r)(\mathbf{v}_2 \cdot \mathbf{e}_r) E' + [(\mathbf{v}_1 \cdot \mathbf{e}_r)^2 + (\mathbf{v}_2 \cdot \mathbf{e}_r)^2] F'\}. \end{aligned} \quad (\text{C20})$$

This can be applied to, e.g., a binary endowed with scalar/vector charges in case that the scalar/vector fields being massless. The Einstein–Infeld–Hoffman Lagrangian corresponds to $A' = B' = C' = D' = E' = 1$ and $F' = 0$. In the COM frame of the binary, the Lagrangian (C20) can be written as

$$\frac{L}{\mu} = G_1 v^2 + G_2 v^4 + G_3 \frac{v^2}{r} + G_4 \frac{\dot{r}^2}{r} + \frac{A}{r} + \frac{B}{r^2}, \quad (\text{C21})$$

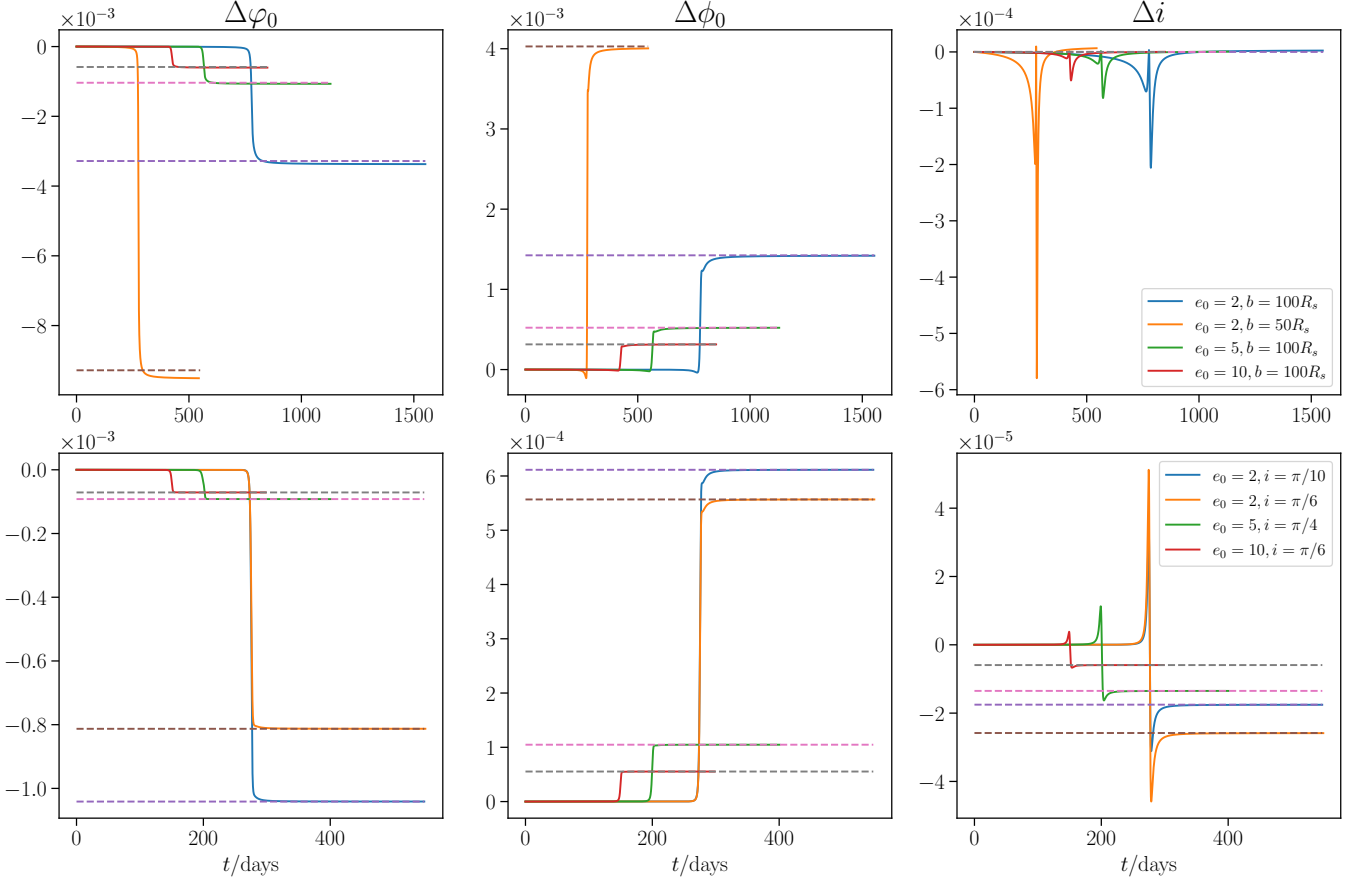


FIG. 11. The variation of angular osculating elements $\Delta\mathcal{X} = \mathcal{X}(t) - \mathcal{X}(0)$ during a hyperbolic encounter under $\mathbf{F}^{(\text{spin})}$ (upper row) with $\varphi_0 = \pi/6$, $J = 0.6 m_1^2$, $i = \pi/6$ and different (e_0, b) , or under $\mathbf{F}^{(\text{quad})}$ (lower row) with $\varphi_0 = \pi/6$, $Q = 10^{-2} M_\odot \text{pc}^2$, $b = 50R_s$ and different (e_0, i) . The analytical approximations (C12), (C13), (C14) and (C15), (C16), (C17) to the total variations are shown as dashed lines.

with $A = A'M$, $B = -B'M^2/2$, $G_1 = 1/2$, $G_2 = (1 - 3\nu)/8$, $G_3/M = 3(1/2 - \nu)C' + (7/2)(D')^2\nu$, $G_4/M = E'\nu/2 + F'(\nu - 1/2)$. From the equation of motion we obtain the acceleration $\mathbf{F}^{(\text{OPN})} = -\frac{A}{2G_1} \frac{\mathbf{e}_r}{r^2}$, and

$$\frac{\mathbf{F}^{(\text{1PN})}}{1/r^2} = \left[(2AG_2 - G_1G_3 - 2G_1G_4)v^2 + 3G_1G_4(\dot{r})^2 + \frac{AG_3 + AG_4 - 2BG_1}{r} \right] \mathbf{e}_r + (4AG_2 + 2G_1G_3) \dot{r} \mathbf{v}. \quad (\text{C22})$$

For an elliptical orbit, the precession angle of the periastron per orbital period $T = 2\pi/\Omega$ is given by

$$\frac{\varphi_0(t+T) - \varphi_0(t)}{T} = -\frac{A[2AG_2 + G_1(2G_3 + G_4)] + 2BG_1^2}{2\sqrt{2a^5 AG_1^5} (e^2 - 1)}. \quad (\text{C23})$$

In the vacuum GR, $\frac{\varphi_0(t+T) - \varphi_0(t)}{T} = \frac{3M^{3/2}}{a^{5/2}(1-e^2)}$. For a hyperbolic orbit, we obtain the change of φ_0 during the scattering:

$$\frac{\Delta\varphi_0}{(AG_1^2 a \sqrt{e^2 - 1})^{-1}} = (4A^2G_2 + 4AG_1G_3 + 2AG_1G_4 + 4BG_1^2) \arctan \frac{e+1}{\sqrt{e^2-1}} - 2A^2G_2 + AG_1G_3 + AG_1G_4 (4A^2G_2 + AG_1G_3 + 2BG_1^2) e^{-2}. \quad (\text{C24})$$

In the vacuum GR, Eq. (C11) is recovered. The results for elliptical and hyperbolic orbits match in the parabolic limit $e = 1$ with $\lim_{\epsilon \rightarrow 0^+} \{[\varphi_0(t+T) - \varphi_0(t)]_{e=1-\epsilon} - (\Delta\varphi_0)_{e=1+\epsilon}\} = 0$.

Finally we consider a power-law radial acceleration: $\mathbf{F} = -Ar^{-n}$, with A and $n \in \mathbb{R}$ being constants. For an

elliptical orbit, we obtain

$$\begin{aligned} \frac{\varphi_0(t+T) - \varphi_0(t)}{T \left(\frac{Aa^{-n}}{2} \right) \sqrt{\frac{a(1-e^2)}{M}}} = \sum_{\lambda=\pm} \left[-(1-\lambda e)^{-n} {}_2F_1 \left(\frac{1}{2}, n; 1; \frac{2e}{e-\lambda} \right) + \lambda \frac{(1-\lambda e)^{-n}}{e} {}_2F_1 \left(\frac{1}{2}, n; 1; \frac{2e}{e-\lambda} \right) \right. \\ \left. + \frac{(1-\lambda e)^{-n}}{(e+\lambda)e} \left\{ [4\lambda e(n-1) + 2] {}_2F_1 \left(\frac{1}{2}, n; 2; \frac{2e}{e-\lambda} \right) + 3\lambda(e-\lambda) {}_2F_1 \left(-\frac{1}{2}, n; 2; \frac{2e}{e-\lambda} \right) \right\} \right], \end{aligned} \quad (\text{C25})$$

where ${}_2F_1(a, b; c; z)$ is the Gauss hypergeometric function. For a hyperbolic orbit, we obtain

$$\begin{aligned} \frac{\Delta\varphi_0}{A \frac{2^n a^3 (ae)^{-n-1} \sqrt{e^2-1}}{n(n^2-1)M}} = -n(n-1) F_1 \left(n+1; n, n; n+2; \frac{i\sqrt{e^2-1}+1}{e}, \frac{e}{i\sqrt{e^2-1}+1} \right) \\ + 2e(n^2-1) F_1 \left(n; n, n; n+1; \frac{i\sqrt{e^2-1}+1}{e}, \frac{e}{i\sqrt{e^2-1}+1} \right) \\ - n(n+1) F_1 \left(n-1; n, n; n; \frac{i\sqrt{e^2-1}+1}{e}, \frac{e}{i\sqrt{e^2-1}+1} \right), \end{aligned} \quad (\text{C26})$$

where $F_1(a; b_1, b_2; c; x, y)$ is the Appell function of the first kind, and the result converges only for $n > 1$. Under $\mathbf{F}^{(1\text{PN})}$ and a conservative radial acceleration (decaying to zero as $r \rightarrow \infty$), the elements $\{a, e, i, \phi_0\}$ of ingoing and outgoing osculating orbits are identical, the deflection angle of the scattering is then given by $2 \arccos(-\frac{1}{e}) - \pi + \Delta\varphi_0$.

-
- [1] B. P. Abbott *et al.* (LIGO Scientific, Virgo), Observation of Gravitational Waves from a Binary Black Hole Merger, *Phys. Rev. Lett.* **116**, 061102 (2016), [arXiv:1602.03837 \[gr-qc\]](#).
 - [2] R. Abbott *et al.* (LIGO Scientific, Virgo), GW190521: A Binary Black Hole Merger with a Total Mass of $150M_\odot$, *Phys. Rev. Lett.* **125**, 101102 (2020), [arXiv:2009.01075 \[gr-qc\]](#).
 - [3] R. Abbott *et al.* (LIGO Scientific, Virgo), GW190814: Gravitational Waves from the Coalescence of a 23 Solar Mass Black Hole with a 2.6 Solar Mass Compact Object, *Astrophys. J. Lett.* **896**, L44 (2020), [arXiv:2006.12611 \[astro-ph.HE\]](#).
 - [4] B. P. Abbott *et al.* (LIGO Scientific, Virgo), GW190425: Observation of a Compact Binary Coalescence with Total Mass $\sim 3.4M_\odot$, *Astrophys. J. Lett.* **892**, L3 (2020), [arXiv:2001.01761 \[astro-ph.HE\]](#).
 - [5] L. Barack and C. Cutler, LISA capture sources: Approximate waveforms, signal-to-noise ratios, and parameter estimation accuracy, *Phys. Rev. D* **69**, 082005 (2004), [arXiv:gr-qc/0310125](#).
 - [6] G.-L. Li, Y. Tang, and Y.-L. Wu, Probing dark matter spikes via gravitational waves of extreme-mass-ratio inspirals, *Sci. China Phys. Mech. Astron.* **65**, 100412 (2022), [arXiv:2112.14041 \[astro-ph.CO\]](#).
 - [7] C. P. L. Berry and J. R. Gair, Expectations for extreme-mass-ratio bursts from the Galactic Centre, *Mon. Not. Roy. Astron. Soc.* **435**, 3521 (2013), [arXiv:1307.7276 \[astro-ph.HE\]](#).
 - [8] M. Turner, Gravitational radiation from point-masses in unbound orbits: Newtonian results., *Astrophys. J.* **216**, 610 (1977).
 - [9] S. Capozziello, M. De Laurentis, F. De Paolis, G. Ingrassio, and A. Nucita, Gravitational waves from hyperbolic encounters, *Mod. Phys. Lett. A* **23**, 99 (2008), [arXiv:0801.0122 \[gr-qc\]](#).
 - [10] S. Capozziello and M. De Laurentis, Gravitational waves from stellar encounters, *Astropart. Phys.* **30**, 105 (2008), [arXiv:0806.4117 \[astro-ph\]](#).
 - [11] J. Garcia-Bellido and S. Nesseris, Gravitational wave bursts from Primordial Black Hole hyperbolic encounters, *Phys. Dark Univ.* **18**, 123 (2017), [arXiv:1706.02111 \[astro-ph.CO\]](#).
 - [12] J. García-Bellido and S. Nesseris, Gravitational wave energy emission and detection rates of Primordial Black Hole hyperbolic encounters, *Phys. Dark Univ.* **21**, 61 (2018), [arXiv:1711.09702 \[astro-ph.HE\]](#).
 - [13] M. Caldarola, S. Kuroyanagi, S. Nesseris, and J. Garcia-Bellido, Effects of orbital precession on hyperbolic encounters, *Phys. Rev. D* **109**, 064001 (2024), [arXiv:2307.00915 \[gr-qc\]](#).
 - [14] W. Junker and G. Schaefer, Binary systems - Higher order gravitational radiation damping and wave emission, *Mon. Not. R. Astron. Soc.* **254**, 146 (1992).
 - [15] R. O. Hansen, Postnewtonian gravitational radiation from point masses in a hyperbolic kepler orbit, *Phys. Rev. D* **5**, 1021 (1972).
 - [16] J. Majar, P. Forgacs, and M. Vasuth, Gravitational waves from binaries on unbound orbits, *Phys. Rev. D* **82**, 064041 (2010), [arXiv:1009.5042 \[gr-qc\]](#).
 - [17] L. De Vittori, A. Gopakumar, A. Gupta, and P. Jetzer, Gravitational waves from spinning compact binaries in hyperbolic orbits, *Phys. Rev. D* **90**, 124066 (2014), [arXiv:1410.6311 \[gr-qc\]](#).

- [18] L. De Vittori, A. Gopakumar, A. Gupta, and P. Jetzer, Memory effect from spinning unbound binaries, *Astrophys. Space Sci. Proc.* **40**, 259 (2015), arXiv:1410.6605 [gr-qc].
- [19] L. De Vittori, A. Gopakumar, A. Gupta, and P. Jetzer, The remains of a spinning, hyperbolic encounter, *J. Phys. Conf. Ser.* **610**, 012048 (2015), arXiv:1410.6606 [gr-qc].
- [20] D. Bini and T. Damour, Gravitational scattering of two black holes at the fourth post-Newtonian approximation, *Phys. Rev. D* **96**, 064021 (2017), arXiv:1706.06877 [gr-qc].
- [21] G. Cho, A. Gopakumar, M. Haney, and H. M. Lee, Gravitational waves from compact binaries in post-Newtonian accurate hyperbolic orbits, *Phys. Rev. D* **98**, 024039 (2018), arXiv:1807.02380 [gr-qc].
- [22] W.-B. Han, X.-Y. Zhong, X. Chen, and S. Xin, Very extreme mass-ratio bursts in the Galaxy and neighbouring galaxies in relation to space-borne detectors, *Mon. Not. Roy. Astron. Soc.* **498**, L61 (2020), arXiv:2004.04016 [gr-qc].
- [23] D. Bini and A. Gerialico, Frequency domain analysis of the gravitational wave energy loss in hyperbolic encounters, *Phys. Rev. D* **104**, 104019 (2021), arXiv:2108.02472 [gr-qc].
- [24] G. Cho, Third post-Newtonian gravitational radiation from two-body scattering. II. Hereditary energy radiation, *Phys. Rev. D* **105**, 104035 (2022), arXiv:2203.10872 [gr-qc].
- [25] A. Roskill, M. Caldarola, S. Kuroyanagi, and S. Nesseris, Mass octupole and current quadrupole corrections to gravitational wave emission from close hyperbolic encounters, *Class. Quant. Grav.* **41**, 235002 (2024), arXiv:2310.07439 [gr-qc].
- [26] J. Fontbuté, T. Andrade, R. Luna, J. C. Bustillo, G. Morrás, S. Jaraba, J. García-Bellido, and G. L. Izquierdo, A numerical-relativity surrogate model for hyperbolic encounters of black holes: challenges in parameter estimation, arXiv e-prints (2024), arXiv:2409.16742 [gr-qc].
- [27] S. Mukherjee, S. Mitra, and S. Chatterjee, Gravitational wave observatories may be able to detect hyperbolic encounters of black holes, *Mon. Not. Roy. Astron. Soc.* **508**, 5064 (2021), arXiv:2010.00916 [gr-qc].
- [28] C. P. L. Berry and J. R. Gair, Extreme-mass-ratio bursts from the Galactic Centre, ASP Conf. Ser. **467**, 185 (2013), arXiv:1209.5731 [astro-ph.HE].
- [29] G. Morrás, J. García-Bellido, and S. Nesseris, Search for black hole hyperbolic encounters with gravitational wave detectors, *Phys. Dark Univ.* **35**, 100932 (2022), arXiv:2110.08000 [astro-ph.HE].
- [30] S. Bini, S. Tiwari, Y. Xu, L. Smith, M. Ebersold, G. Principe, M. Haney, P. Jetzer, and G. A. Prodi, Search for hyperbolic encounters of compact objects in the third LIGO-Virgo-KAGRA observing run, *Phys. Rev. D* **109**, 042009 (2024), arXiv:2311.06630 [gr-qc].
- [31] J. García-Bellido, S. Jaraba, and S. Kuroyanagi, The stochastic gravitational wave background from close hyperbolic encounters of primordial black holes in dense clusters, *Phys. Dark Univ.* **36**, 101009 (2022), arXiv:2109.11376 [gr-qc].
- [32] M. Kerachian, S. Mukherjee, G. Lukes-Gerakopoulos, and S. Mitra, Detectability of stochastic gravitational wave background from weakly hyperbolic encounters, *Astron. Astrophys.* **684**, A17 (2024), arXiv:2311.16634 [gr-qc].
- [33] S. Dandapat, A. Susobhanan, L. Dey, A. Gopakumar, P. T. Baker, and P. Jetzer, Efficient prescription to search for linear gravitational wave memory from hyperbolic black hole encounters and its application to the NANOGrav 12.5-year dataset, *Phys. Rev. D* **109**, 103018 (2024), arXiv:2402.03472 [astro-ph.HE].
- [34] B. Kocsis, N. Yunes, and A. Loeb, Observable Signatures of EMRI Black Hole Binaries Embedded in Thin Accretion Disks, *Phys. Rev. D* **84**, 024032 (2011), arXiv:1104.2322 [astro-ph.GA].
- [35] G. Bertone *et al.*, Gravitational wave probes of dark matter: challenges and opportunities, *SciPost Phys. Core* **3**, 007 (2020), arXiv:1907.10610 [astro-ph.CO].
- [36] V. Cardoso, C. F. B. Macedo, and R. Vicente, Eccentricity evolution of compact binaries and applications to gravitational-wave physics, *Phys. Rev. D* **103**, 023015 (2021).
- [37] N. Becker, L. Sagunski, L. Prinz, and S. Rastgoo, Circularization versus eccentricification in intermediate mass ratio inspirals inside dark matter spikes, *Phys. Rev. D* **105**, 063029 (2022), arXiv:2112.09586 [gr-qc].
- [38] V. Cardoso, K. Destounis, F. Duque, R. P. Macedo, and A. Maselli, Black holes in galaxies: Environmental impact on gravitational-wave generation and propagation, *Phys. Rev. D* **105**, L061501 (2022), arXiv:2109.00005 [gr-qc].
- [39] V. Cardoso, K. Destounis, F. Duque, R. Panosso Macedo, and A. Maselli, Gravitational Waves from Extreme-Mass-Ratio Systems in Astrophysical Environments, *Phys. Rev. Lett.* **129**, 241103 (2022), arXiv:2210.01133 [gr-qc].
- [40] N. Becker and L. Sagunski, Comparing accretion disks and dark matter spikes in intermediate mass ratio inspirals, *Phys. Rev. D* **107**, 083003 (2023), arXiv:2211.05145 [gr-qc].
- [41] X.-J. Yue and W.-B. Han, Gravitational waves with dark matter minispikes: the combined effect, *Phys. Rev. D* **97**, 064003 (2018), arXiv:1711.09706 [gr-qc].
- [42] X.-J. Yue, W.-B. Han, and X. Chen, Dark matter: an efficient catalyst for intermediate-mass-ratio-inspiral events, *Astrophys. J.* **874**, 34 (2019), arXiv:1802.03739 [gr-qc].
- [43] E. Barausse, V. Cardoso, and P. Pani, Can environmental effects spoil precision gravitational-wave astrophysics?, *Phys. Rev. D* **89**, 104059 (2014), arXiv:1404.7149 [gr-qc].
- [44] P. S. Cole, G. Bertone, A. Coogan, D. Gaggero, T. Karydas, B. J. Kavanagh, T. F. M. Spieksma, and G. M. Tomaselli, Distinguishing environmental effects on binary black hole gravitational waveforms, *Nature Astron.* **7**, 943 (2023), arXiv:2211.01362 [gr-qc].
- [45] M. Rahman, S. Kumar, and A. Bhattacharyya, Probing astrophysical environment with eccentric extreme mass-ratio inspirals, *JCAP* **01**, 035, arXiv:2306.14971 [gr-qc].
- [46] G. Bertone, Dark matter, black holes, and gravitational waves, *Nucl. Phys. B* **1003**, 116487 (2024), arXiv:2404.11513 [astro-ph.CO].
- [47] X.-J. Yue and Z. Cao, Dark matter minispikes: A significant enhancement of eccentricity for intermediate-mass-ratio inspirals, *Phys. Rev. D* **100**, 043013 (2019), arXiv:1908.10241 [astro-ph.HE].
- [48] X.-J. Yue and Z. Cao, Gravitational waves with dark matter minispikes: Fourier-domain waveforms of eccentric intermediate-mass-ratio-inspirals, *Class. Quant. Grav.* **41**, 095011 (2024).
- [49] Z.-C. Zhang and Y. Tang, Velocity Distribution of Dark

- Matter Spike around Schwarzschild Black Holes and Effects on Gravitational Waves from EMRIs, arXiv e-prints (2024), [arXiv:2403.18529 \[astro-ph.GA\]](#).
- [50] D. Montalvo, A. Smith-Orlik, S. Rastgoo, L. Sagunski, N. Becker, and H. Khan, Post-Newtonian effects in compact binaries with a dark matter spike: A Lagrangian approach, arXiv e-prints (2024), [arXiv:2401.06084 \[gr-qc\]](#).
- [51] C. Zhang, G. Fu, and Y. Gong, The constraint on modified black holes with extreme mass ratio inspirals, arXiv e-prints (2024), [arXiv:2408.15064 \[gr-qc\]](#).
- [52] Y. Zhao, N. Dai, and Y. Gong, Distinguishing dark matter halos with Extreme mass ratio inspirals, arXiv e-prints (2024), [arXiv:2410.06882 \[gr-qc\]](#).
- [53] N. Speeney, E. Berti, V. Cardoso, and A. Maselli, Black holes surrounded by generic matter distributions: Polar perturbations and energy flux, *Phys. Rev. D* **109**, 084068 (2024), [arXiv:2401.00932 \[gr-qc\]](#).
- [54] F. Duque, C. F. B. Macedo, R. Vicente, and V. Cardoso, Extreme-Mass-Ratio Inspirals in Ultralight Dark Matter, *Phys. Rev. Lett.* **133**, 121404 (2024), [arXiv:2312.06767 \[gr-qc\]](#).
- [55] A. Chowdhuri, R. K. Singh, K. Kangsabanik, and A. Bhattacharyya, Gravitational radiation from hyperbolic encounters in the presence of dark matter, *Phys. Rev. D* **109**, 124056 (2024), [arXiv:2306.11787 \[gr-qc\]](#).
- [56] S. Albanesi, A. Rashti, F. Zappa, R. Gamba, W. Cook, B. Daszuta, S. Bernuzzi, A. Nagar, and D. Radice, Scattering and dynamical capture of two black holes: synergies between numerical and analytical methods, arXiv e-prints (2024), [arXiv:2405.20398 \[gr-qc\]](#).
- [57] H. Mouri and Y. Taniguchi, Runaway merging of black holes: analytical constraint on the timescale, *Astrophys. J. Lett.* **566**, L17 (2002), [arXiv:astro-ph/0201102](#).
- [58] R. R. Bate, D. D. Mueller, and J. E. White, *Fundamentals of Astrodynamics* (Dover Publications, 1971).
- [59] L. Blanchet, Post-Newtonian Theory for Gravitational Waves, *Living Rev. Rel.* **17**, 2 (2014), [arXiv:1310.1528 \[gr-qc\]](#).
- [60] J. Vines, Scattering of two spinning black holes in post-Minkowskian gravity, to all orders in spin, and effective-one-body mappings, *Class. Quant. Grav.* **35**, 084002 (2018), [arXiv:1709.06016 \[gr-qc\]](#).
- [61] T. Damour, Classical and quantum scattering in post-Minkowskian gravity, *Phys. Rev. D* **102**, 024060 (2020), [arXiv:1912.02139 \[gr-qc\]](#).
- [62] D. Bini, A. Geralico, and J. Vines, Hyperbolic scattering of spinning particles by a Kerr black hole, *Phys. Rev. D* **96**, 084044 (2017), [arXiv:1707.09814 \[gr-qc\]](#).
- [63] P. Gondolo and J. Silk, Dark matter annihilation at the galactic center, *Phys. Rev. Lett.* **83**, 1719 (1999), [arXiv:astro-ph/9906391](#).
- [64] P. Ullio, H. Zhao, and M. Kamionkowski, A Dark matter spike at the galactic center?, *Phys. Rev. D* **64**, 043504 (2001), [arXiv:astro-ph/0101481](#).
- [65] O. Y. Gnedin and J. R. Primack, Dark matter profile in the galactic center, *Phys. Rev. Lett.* **93**, 061302 (2004).
- [66] L. Sadeghian, F. Ferrer, and C. M. Will, Dark matter distributions around massive black holes: A general relativistic analysis, *Phys. Rev. D* **88**, 063522 (2013), [arXiv:1305.2619 \[astro-ph.GA\]](#).
- [67] O. A. Hannuksela, K. C. Y. Ng, and T. G. F. Li, Extreme dark matter tests with extreme mass ratio inspirals, *Phys. Rev. D* **102**, 103022 (2020), [arXiv:1906.11845 \[astro-ph.CO\]](#).
- [68] B. J. Kavanagh, D. A. Nichols, G. Bertone, and D. Gaggero, Detecting dark matter around black holes with gravitational waves: Effects of dark-matter dynamics on the gravitational waveform, *Phys. Rev. D* **102**, 083006 (2020), [arXiv:2002.12811 \[gr-qc\]](#).
- [69] E. P. Lee, Dynamical Friction in the Post-Newtonian Approximation of General Relativity, *Astrophys. J.* **155**, 687 (1969).
- [70] C. Chiari and P. Di Cintio, Relativistic dynamical friction in stellar systems, *Astron. Astrophys.* **677**, A140 (2023), [arXiv:2207.05728 \[astro-ph.GA\]](#).
- [71] F. Dosopoulou, Dynamical friction in dark matter spikes: Corrections to Chandrasekhar's formula, *Phys. Rev. D* **110**, 083027 (2024), [arXiv:2305.17281 \[astro-ph.HE\]](#).
- [72] S. Chandrasekhar, Dynamical Friction. I. General Considerations: the Coefficient of Dynamical Friction, *Astrophys. J.* **97**, 255 (1943).
- [73] J. Frank, A. King, and D. Raine, *Accretion Power in Astrophysics*, 3rd ed. (Cambridge University Press, Cambridge, UK, 2002).
- [74] F. J. Sánchez-Salcedo, Orbital Evolution of Gas-driven Inspirals with Extreme Mass Ratios: Retrograde Eccentric Orbits, *Astrophys. J.* **897**, 142 (2020), [arXiv:2006.10206 \[astro-ph.GA\]](#).
- [75] J.-R. Liu, Y.-L. Wang, and J.-M. Wang, Accretion-modified Stars in Accretion Disks of Active Galactic Nuclei: Observational Characteristics in Different Regions of the Disks, *Astrophys. J.* **969**, 37 (2024), [arXiv:2405.02855 \[astro-ph.HE\]](#).
- [76] J. Goodman and J. C. Tan, Supermassive Stars in Quasar Disks, *Astrophys. J.* **608**, 108 (2004), [arXiv:astro-ph/0307361 \[astro-ph\]](#).
- [77] J. Goodman and J. C. Tan, Supermassive stars in quasar disks, *Astrophys. J.* **608**, 108 (2004), [arXiv:astro-ph/0307361](#).
- [78] E. C. Ostriker, Dynamical Friction in a Gaseous Medium, *Astrophys. J.* **513**, 252 (1999), [arXiv:astro-ph/9810324 \[astro-ph\]](#).
- [79] M. Xiang-Gruess and J. C. B. Papaloizou, Interaction between massive planets on inclined orbits and circumstellar discs, *Mon. Not. R. Astron. Soc.* **431**, 1320 (2013), [arXiv:1302.2045 \[astro-ph.EP\]](#).
- [80] J. Binney and S. Tremaine, *Galactic Dynamics*, 2nd ed. (Princeton University Press, Princeton, NJ, 2008).
- [81] M. Maggiore, *Gravitational Waves: Volume 1: Theory and Experiments* (Oxford University Press, 2008).
- [82] C. Cutler, Angular resolution of the LISA gravitational wave detector, *Phys. Rev. D* **57**, 7089 (1998), [arXiv:gr-qc/9703068](#).
- [83] T. Robson, N. J. Cornish, and C. Liu, The construction and use of LISA sensitivity curves, *Class. Quant. Grav.* **36**, 105011 (2019), [arXiv:1803.01944 \[astro-ph.HE\]](#).
- [84] R. Bender, J. Kormendy, G. Bower, R. Green, J. Thomas, A. C. Danks, T. Gull, J. B. Hutchings, C. L. Joseph, M. E. Kaiser, T. R. Lauer, C. H. Nelson, D. Richstone, D. Weistrop, and B. Woodgate, HST STIS Spectroscopy of the Triple Nucleus of M31: Two Nested Disks in Keplerian Rotation around a Supermassive Black Hole, *Astrophys. J.* **631**, 280 (2005), [arXiv:astro-ph/0509839 \[astro-ph\]](#).
- [85] I. D. Karachentsev, V. E. Karachentseva, W. K. Huchtmeier, and D. I. Makarov, A Catalog of Neighboring Galaxies, *Astron. J.* **127**, 2031 (2004).

- [86] L. Meyer, A. M. Ghez, R. Schödel, S. Yelda, A. Boehle, J. R. Lu, T. Do, M. R. Morris, E. E. Becklin, and K. Matthews, The Shortest-Known-Period Star Orbiting Our Galaxy's Supermassive Black Hole, *Science* **338**, 84 (2012), [arXiv:1210.1294 \[astro-ph.GA\]](#).
- [87] G. M. Tomaselli, T. F. M. Spieksma, and G. Bertone, Dynamical friction in gravitational atoms, *JCAP* **07**, 070, [arXiv:2305.15460 \[gr-qc\]](#).
- [88] Y. Cao and Y. Tang, Signatures of ultralight bosons in compact binary inspiral and outspiral, *Phys. Rev. D* **108**, 123017 (2023), [arXiv:2307.05181 \[gr-qc\]](#).
- [89] Y.-Z. Cheng, W.-H. Wu, and Y. Cao, Electromagnetic Radiation from Binary Stars Mediated by Ultralight Scalar, *arXiv e-prints* (2023), [arXiv:2401.00204 \[astro-ph.CO\]](#).
- [90] H. D. Curtis, *Orbital Mechanics for Engineering Students*, 4th ed. (Elsevier, Oxford, UK, 2020).
- [91] N. I. Shakura and R. A. Sunyaev, Black Holes in Binary Systems: Observational Appearances, in *X- and Gamma-Ray Astronomy*, IAU Symposium, Vol. 55, edited by H. Bradt and R. Giacconi (1973) p. 155.
- [92] J. A. Kollmeier *et al.*, Black hole masses and eddington ratios at $0.3 < z < 4$, *Astrophys. J.* **648**, 128 (2006), [arXiv:astro-ph/0508657](#).
- [93] J. Goodman, Self-gravity and quasi-stellar object discs, *Mon. Not. R. Astron. Soc.* **339**, 937 (2003), [arXiv:astro-ph/0201001 \[astro-ph\]](#).
- [94] L. E. Kidder, Coalescing binary systems of compact objects to (post)^{5/2}-newtonian order. v. spin effects, *Phys. Rev. D* **52**, 821 (1995).
- [95] E. Poisson, Gravitational waves from inspiraling compact binaries: The Quadrupole moment term, *Phys. Rev. D* **57**, 5287 (1998), [arXiv:gr-qc/9709032](#).
- [96] T. Mora and C. M. Will, A PostNewtonian diagnostic of quasiequilibrium binary configurations of compact objects, *Phys. Rev. D* **69**, 104021 (2004), [Erratum: *Phys.Rev.D* 71, 129901 (2005)], [arXiv:gr-qc/0312082](#).
- [97] T. Damour and N. Deruelle, General relativistic celestial mechanics of binary systems. I. The post-Newtonian motion., *Annales de L'Institut Henri Poincare Section (A) Physique Theorique* **43**, 107 (1985).
- [98] B. Cashen, A. Aker, and M. Kesden, Gravitomagnetic dynamical friction, *Phys. Rev. D* **95**, 064014 (2017).